
Measurement of the Inclusive Cross Section of
 ρ^0 , $f_0(980)$ and $f_2(1270)$ Mesons in Deep
Inelastic Scattering at HERA

Andrée Robichaud-Véronneau
High Energy Physics
Department of Physics
McGill University
Montréal, Québec
Canada

August 2005

A thesis submitted to
McGill University
in partial fulfillment of the requirements for the degree of
Master of Science

© Andrée Robichaud-Véronneau, 2005



Library and
Archives Canada

Bibliothèque et
Archives Canada

Published Heritage
Branch

Direction du
Patrimoine de l'édition

395 Wellington Street
Ottawa ON K1A 0N4
Canada

395, rue Wellington
Ottawa ON K1A 0N4
Canada

Your file *Votre référence*
ISBN: 978-0-494-24781-5
Our file *Notre référence*
ISBN: 978-0-494-24781-5

NOTICE:

The author has granted a non-exclusive license allowing Library and Archives Canada to reproduce, publish, archive, preserve, conserve, communicate to the public by telecommunication or on the Internet, loan, distribute and sell theses worldwide, for commercial or non-commercial purposes, in microform, paper, electronic and/or any other formats.

The author retains copyright ownership and moral rights in this thesis. Neither the thesis nor substantial extracts from it may be printed or otherwise reproduced without the author's permission.

AVIS:

L'auteur a accordé une licence non exclusive permettant à la Bibliothèque et Archives Canada de reproduire, publier, archiver, sauvegarder, conserver, transmettre au public par télécommunication ou par l'Internet, prêter, distribuer et vendre des thèses partout dans le monde, à des fins commerciales ou autres, sur support microforme, papier, électronique et/ou autres formats.

L'auteur conserve la propriété du droit d'auteur et des droits moraux qui protègent cette thèse. Ni la thèse ni des extraits substantiels de celle-ci ne doivent être imprimés ou autrement reproduits sans son autorisation.

In compliance with the Canadian Privacy Act some supporting forms may have been removed from this thesis.

Conformément à la loi canadienne sur la protection de la vie privée, quelques formulaires secondaires ont été enlevés de cette thèse.

While these forms may be included in the document page count, their removal does not represent any loss of content from the thesis.

Bien que ces formulaires aient inclus dans la pagination, il n'y aura aucun contenu manquant.


Canada

Abstract

The production of neutral meson resonances in deep inelastic scattering has been studied in DESY with the ZEUS detector at the HERA collider. The ρ^0 , $f_0(980)$ and $f_2(1270)$ total cross sections, as well as differential p_T and η cross sections, were measured in the $0 \text{ GeV} < p_T < 7 \text{ GeV}$ and $|\eta| < 1$ ranges. The obtained total cross sections were $\sigma_{\rho^0} = 19.21 \pm 0.92 \text{ (stat.)} \pm 7.59 \text{ (syst.) nb}$, $\sigma_{f_0} = 0.63 \pm 0.04 \text{ (stat.)} \pm 0.25 \text{ (syst.) nb}$ and $\sigma_{f_2} = 3.62 \pm 0.02 \text{ (stat.)} \pm 1.73 \text{ (syst.) nb}$. The cross sections measurements for f_0 and f_2 mesons are underestimated since acceptances had to be overestimated. The measurements were performed on a data sample with 82.5 nb^{-1} of integrated luminosity and for a squared momentum transfer greater than 3 GeV^2 .

Résumé

La production de résonances mésoniques neutres en collisions inélastiques profondes a été étudiée à DESY avec le détecteur ZEUS au collisionneur HERA. Les sections efficaces totales et différentielles en fonction de p_T et η des mésons ρ^0 , $f_0(980)$ et $f_2(1270)$ ont été mesurées dans les intervalles $0 \text{ GeV} < p_T < 7 \text{ GeV}$ ainsi que $|\eta| < 1$. Les sections efficaces totales obtenues sont $\sigma_{\rho^0} = 19,21 \pm 0,92 \text{ (stat.)} \pm 7,59 \text{ (syst.) nb}$, $\sigma_{f_0} = 0,63 \pm 0,04 \text{ (stat.)} \pm 0,25 \text{ (syst.) nb}$ et $\sigma_{f_2} = 3,62 \pm 0,02 \text{ (stat.)} \pm 1,73 \text{ (syst.) nb}$. Les sections efficaces pour les mésons f_0 et f_2 sont sous-estimées car les acceptances ont dû être surestimées. Les mesures ont été effectuées sur un échantillon de données de $82,5 \text{ nb}^{-1}$ de luminosité intégrée et pour une valeur du carré de la quantité de mouvement échangée supérieure à 3 GeV^2 .

Contents

List of figures	iii
List of tables	iv
Acknowledgements	v
1 Introduction	1
2 Neutral Meson Resonance Production in DIS	3
2.1 Quark Parton Model (QPM)	3
2.2 QCD and The Standard Model	5
2.3 Event Kinematics	7
2.4 Perturbative QCD	9
2.5 QCD Improved QPM	12
2.6 Deep Inelastic Scattering	17
2.7 Resonance Production	18
2.8 From Theory to Experiment	20
3 ZEUS: A Detector for HERA	23
3.1 HERA: die “Hadron Elektron Ring Anlage”	23
3.2 The ZEUS Detector	25
3.2.1 The Central Tracking Detector (CTD)	27
3.2.2 Vertex and Track Reconstruction	28
3.2.3 The Uranium Calorimeter (CAL)	29
3.2.4 The Luminosity Monitor	31
3.3 Data Acquisition and Trigger	32
4 Event Selection	35
4.1 Online Event Selection	35
4.1.1 First Level Trigger	37
4.1.2 Second Level Trigger	37
4.1.3 Third Level Trigger	38
4.2 Offline Event Selection	39
4.2.1 Calorimeter Noise and ‘Sparks’ Suppression	40
4.2.2 Photoproduction Background	40

4.3	Cleaning Cuts	40
4.3.1	Vertex Position	41
4.3.2	Transverse Momentum	41
4.3.3	Angular Distribution	42
4.3.4	Phase Space	42
5	Event Simulation	45
5.1	Event Generation	45
5.2	ARIADNE-flavoured DJANGO	46
5.3	Detector Simulation	47
5.4	DIS Sample	48
6	Meson Production Analysis	49
6.1	Monte Carlo vs Data	49
6.1.1	Control Plots	49
6.1.2	Monte Carlo Reweighting	50
6.2	Signal Extraction	53
6.2.1	Reflections	53
6.2.2	Invariant Mass Spectrum	55
6.3	Detector Corrections	59
6.4	Cross Section Measurement	61
6.4.1	Total Cross Sections	61
6.4.2	Differential p_T Cross Sections	62
6.4.3	Differential η Cross Sections	66
6.4.4	Systematic Uncertainties	66
6.5	Discussion	69
7	Conclusion and Outlook	71
	Glossary	73
	References	76

List of Figures

2.1	The Eightfold Way	3
2.2	Representation of Bjorken x	8
2.3	Feynman diagram example	9
2.4	The structure function as a function of x	13
2.5	Measurement of F_2	14
2.6	Kinematic region coverage	16
2.7	NC and CC Feynman diagrams	18
2.8	ρ^0 production	19
2.9	H1 plot for double differential cross sections	20
3.1	The HERA accelerator	24
3.2	The ZEUS detector	25
3.3	A CTD octant	27
3.4	Side overview of the Calorimeter	29
3.5	CAL cells layout	30
3.6	The luminosity monitor	31
3.7	ZEUS trigger chain	33
4.1	Event production and analysis chain in ZEUS	36
4.2	Vertex position	41
4.3	Q^2 and $E-p_z$ cuts	43
5.1	Three phases of event generation	46
6.1	Control plots before reweighting	50
6.2	Monte Carlo reweighting	51
6.3	Monte Carlo reweighted	52
6.4	Reflections invariant mass plot	54
6.5	2-track invariant mass spectrum	56
6.6	Fit of the 2-track invariant mass spectrum	58
6.7	Mass distributions per p_T bin	64
6.8	Differential p_T cross sections	65
6.9	Differential η cross sections	67
6.10	H1 differential cross sections	70

List of Tables

2.1	The Standard Model - Matter	6
2.2	The Standard Model - Forces	6
4.1	TLT prescale and cuts for 1998-2000	39
6.1	Fit parameters for the three mesons	59
6.2	Acceptances for the three mesons	60
6.3	Differential cross sections in p_T	63
6.4	Differential cross sections in η	66

Acknowledgements

Before letting you dive into the wonderful world of high energy physics, I would like to take a few lines to thank all the people who contributed to the achievement of this work.

First and foremost, thanks to the QCD group, in particular Sergei Chekanov and Amita Raval, for helping me in the analysis. Thanks to my supervisor, Prof. François Corriveau, for giving me this great opportunity to work in DESY. Thanks to Roberval Walsh for his time and dedication. Special thanks to my colleagues Sanjay, Sebastian and Mathieu, for invaluable help, time and laughs; working with you was a great pleasure. I would also like to thank all the people from the CAL group, Thomas Schörner, Alessandro Polini, Wladimir Hain, Bill Schmidke and Cathy Farrow, for making me enjoy the hardware work as much as the analysis.

Of course, life in Hamburg would definitely not have been the same without the DPC, in particular Bob, Pat, Freddy, Simon, Ricardo, Paul, Matt and Dave. Thank you, great people from the Cranachstrasse, Nuala, Wojtek(s), Marcin, Michele, Iulia, Jamie, Anita, Valeria, and of course, Sophie and Uwe.

While I was in Hamburg, people were supporting me from Canada. Thanks specially to Thomas, Chris and to all the others that I am surely forgetting!

Finally, I would like to thank my father, for his great patience and support and Olivier, without whom life would have no meaning.

1 Introduction

In 2004, the Nobel prize of Physics was given to three theoretical physicists, David Gross, Frank Wilczek and David Politzer, for their work on Quantum Chromodynamics (QCD) and especially on asymptotic freedom. This was also due to the incredible work of thousands of physicists over 30 years to bring experimental proof that the theory was indeed describing nature.

This is especially true at the research center DESY with HERA, the first ep collider in the world. In particular, with the ZEUS detector, it is possible to study many aspects of QCD, including neutral particle production, which is the subject of this thesis. The production of three neutral mesons, ρ^0 , $f_0(980)$ and $f_2(1270)$, is presented here. The measurement of their cross sections can shed light on the difficult subject of hadronisation, since high energy collisions with high particle multiplicities represent a good opportunity to do so. The combination of quarks and gluons to form colorless hadrons is still not understood and cannot be described by perturbative QCD, which is the main tool of particle physicists for the strong interactions. The production of neutral meson resonances can also be interesting in order to look for regularities in the particle spectra and to compare short-lived particles, or *resonances*, with long-lived hadrons. In order to achieve this, the differential cross sections of several particles should be studied. This thesis is a first attempt to do this measurement for these three mesons in deep inelastic measurement at ZEUS.

First, an outline of the underlying theory, QCD, is presented, with aspects of meson resonance production. Then the ZEUS detector and its components relevant to this analysis are described. A description of the criteria for event selection is done in section 4 and the overview of the data simulation used for comparison of data with theoretical models is in the following section. Finally, the meson production analysis is presented in section 6, with total and differential cross-section measurements.

2 Neutral Meson Resonance Production in DIS

In 1973, Gross, Wilczek and Politzer published two articles [1], throwing the bases for a non-abelian gauge theory of the strong interactions that would also exhibit asymptotic freedom. This theory is now commonly known as Quantum Chromodynamics (QCD) and is the basis for the work done at experiments such as ZEUS. In this section, the theory will be outlined and aspects of it that are more relevant to the present analysis will be developed. Also, details of resonance production and the deep inelastic regime in ep collisions will be presented.

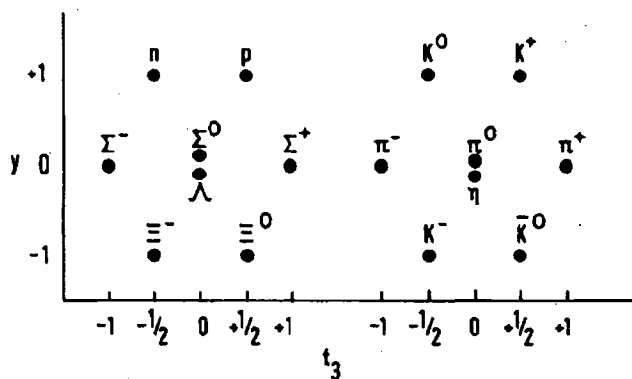


Figure 2.1: *Weight diagrams for the $J^P = \frac{1}{2}^+$ baryon octet and the pseudoscalar meson octet in the Eightfold Way. On the axes, y is the hypercharge eigenvalue and t_3 is the isospin eigenvalue.*

2.1 Quark Parton Model (QPM)

In the 20th century, thanks to the work done by many brilliant physicists, quantum mechanics was made a reality. Soon enough, the combination of quantum physics and relativity was achieved and field theory was born. This brought a whole new field of experimental physics to life: the study of elementary particles. In the 1950's, the detection of unknown particles, all believed to be fundamental, led to "the particle zoo", a collection of particles for which no substructure was known. Some ordering and understanding had to be done, otherwise particle physics was starting to become "stamp collecting" in Rutherford's words [2].

In a first attempt to classify these new results, Gell-Mann and independently Ne’eman, developed a classification scheme called the “Eightfold Way”, as shown in figure 2.1, in which the hadrons were grouped according to their quantum numbers, e.g. strangeness and isospin, into multiplets of the symmetry group $SU(3)$, following certain patterns. This model could predict the existence and the quantum numbers of particles not yet discovered at the time. These particles were not, in that model, considered to be bound states of quarks, although the name *quark* was brought up by Gell-Mann to be purely theoretical subcomponents of the hadrons [3].

In the late 1960’s, at the SLAC-MIT experiment, which was a fixed target electron-nucleon scattering experiment¹, an important breakthrough was made with the help of two theorists: Feynman and Bjorken. The idea of this scattering experiment was similar to the Rutherford scattering experiment; here, electrons were like alpha particles and protons were playing the role of the nuclei. The results were showing that the charge was not distributed uniformly in the proton, contrarily to the previous results of lower energy experiments. Bjorken then proposed that there might be a *scaling effect* for different electron energies. Feynman interpreted this effect as *partons*, i.e. point-like subcomponents of the proton, hence the quark-parton model was born. The proton was then nothing more than a bunch of quarks with low momentum transverse to the proton’s momentum, forming a bound state. According to this theory, the differential ep cross-section was defined as follows [4]:

$$\frac{d^2\sigma}{dQ^2 d\nu} = \frac{\pi}{EE'} \frac{\alpha^2}{4EE' \sin^4 \frac{\theta}{2}} \left[2W_1(x, Q^2) \sin^2 \frac{\theta}{2} + W_2(x, Q^2) \cos^2 \frac{\theta}{2} \right] \quad (2.1)$$

The variables E , E' and θ refer respectively to the electron incident and scattered energy and scattering angle and α is the fine structure constant. The functions W_1 and W_2 are dimensionless structure functions, meant to describe the partonic substructure. They can be expressed in more simple terms by defining the following new structure functions F_1 and F_2 .

¹ Electrons were scattering off hydrogen atoms in a liquid H target.

$$\begin{aligned} F_1 &\equiv M_p W_1 \\ F_2 &\equiv \nu W_2 \end{aligned} \tag{2.2}$$

Q^2 , ν and x will be defined in section 2.3. F_1 measures the parton density and F_2 , the momentum density. M_p is the proton mass. These densities were believed initially to depend on x and Q^2 . But further measurements of the F_2 structure function showed a dependence on x only [5], exhibiting a scaling behaviour, known as *Bjorken scaling*. F_2 could now be expressed as:

$$F_2(x) = x \sum_i e_i^2 f_i(x) + x \sum_i e_i^2 \bar{f}_i(x) \tag{2.3}$$

where the sums run over all quark flavours, e is the electric charge of the partons and f is the number of quarks of each flavour within a range dx of the proton momentum (\bar{f} is the anti-particle equivalent). This is a naïve picture of the proton made of point-like partons. If the partons were spin- $\frac{1}{2}$ particles, it was further proved by Callan and Gross that the following should hold [6]:

$$2xF_1(x) = F_2(x) \tag{2.4}$$

Experimental data did confirm equation 2.4, hence proving that the partons were indeed spin- $\frac{1}{2}$ particles. It was the experimental proof and first application of Gell-Mann's *quarks*, the hypothetical SU(3) particles of the Eightfold way, as the proton constituents [7].

This picture soon would need the help of QCD to be complete. The next section outlines the theory of the strong interactions.

2.2 QCD and The Standard Model

With the quark description of the proton, particle physicists came up with a better and more fundamental picture of matter and forces, which is known as the Standard Model. It is, so far, a very accurate model of the particles and interactions of nature. It is presented in tables 2.1 and 2.2.

Constituents of matter					
Quarks			Leptons		
1 st gen.	2 nd gen.	3 rd gen.	1 st gen.	2 nd gen.	3 rd gen.
u	c	t	e	μ	τ
d	s	b	ν_e	ν_μ	ν_τ

Table 2.1: *The Constituents of Matter in the Standard Model. The quarks and the leptons are classified in three generations of increasing particle masses.*

In the Standard Model, the quarks and the leptons form matter and the force carrier bosons serve as mediators for the four fundamental forces. QCD is concerned with the strong force, describing the interactions between quarks and gluons. Similarly to the electric charge in QED (Quantum Electrodynamics), the quarks and the gluons carry a *color charge* which comes in three varieties: r (red), g (green), b (blue) and their three associated anti-colors. There are then eight types of gluons, each carrying a color doublet. Since, at a strong vertex, a quark can change color, the gluon will carry off the difference, which forms a color doublet.

Fundamental Forces	Force Carriers
Strong	Gluon (g)
Electromagnetic	Photon (γ)
Weak	W & Z
Gravity	Graviton

Table 2.2: *The Fundamental Forces in the Standard Model*

The notion of color was introduced with the discovery of the Δ^{++} baryon [8], which was believed to be made of three *u*-quarks with total angular momentum $J=3/2$, while quarks have spin $J=1/2$. For this to happen, the quark model had to violate Pauli exclusion principle to allow three identical particles with their spin aligned to be in the same state. With the color charge, introduced by Greenberg in 1964 [9], these three quarks were in three different color states, solving the mystery and keeping a very basic principle of physics intact!

If every strong interacting particle carries a color charge, all the observed hadrons are *colorless* or *color neutral*, being either baryons (with an antisymmetric color wavefunction) or mesons (color-anti-color pairs). This fact leads to the *confinement* hypothesis, which states that colored particles (e.g. free quarks and gluons) cannot be observed directly. If so, they would have infinite energy at large distances, the so-called *Infrared Divergencies* (IR).

Compared to QED, QCD is more complicated in many aspects. One of them is the size of the coupling constant. In the first case, the fine structure constant is small enough to allow neglect of higher order effects ($\alpha \sim \frac{1}{137}$). In the second case, the strong coupling constant is a "running constant" (i.e. depending on the energy). The running of α_s is such that it is inversely proportional to the energy. The consequence of that fact is called *asymptotic freedom*. More practically, it means that at large distances compared to the quark size, the coupling increases and that at short distances ($\mathcal{O}(10^{-16}$ m)), it decreases such that the quarks and gluons can be treated as free particles, allowing perturbation theory to be used.

2.3 Event Kinematics

Many variables characterize the kinematics in a lepton-nucleon scattering event. Let l be the momentum of the incoming lepton, l' the momentum of the scattered lepton, p the incoming proton's momentum and q the momentum of the exchanged boson ($q = l - l'$). Using these, one can express the center-of-mass energy \sqrt{s} as follows, where E_e and E_p are the incident particles energies:

$$s = (l + p)^2 = 4E_e E_p \quad (2.5)$$

One of the most important variables is the squared four-momentum transfer which is carried by the virtual boson, the Lorentz invariant Q^2 . It is also known as the virtuality of the exchanged boson and is defined by:

$$Q^2 = -q^2 = -(l - l')^2 \quad (2.6)$$

It is used to distinguish between the two kinematic regimes in ep scattering: DIS and photoproduction. A photoproduction event is characterized by $Q^2 \lesssim 1 \text{ GeV}^2$. Contrarily, a DIS event has $Q^2 \gtrsim 1 \text{ GeV}^2$.

The momentum transfer is also a measure of the size of the probed structure inside the proton. The resolving power of the probe is related to its energy using $q \propto \frac{1}{\lambda}$, where λ is the De Broglie wavelength of the probe and q is the momentum transfer. As Q^2 grows larger, it is then possible to “see” smaller structure and as $Q^2 \rightarrow \infty$, the partons should behave as free particles.

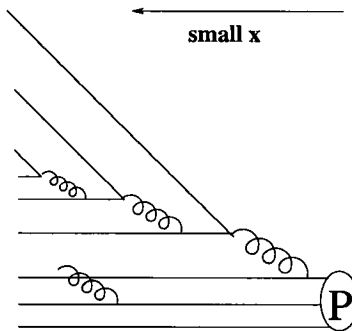


Figure 2.2: Schematic representation of Bjorken x inside the proton. As x decreases, the density of sea quarks originating from gluon splittings increases.

Another important variable is the Bjorken scaling variable, commonly known as *Bjorken x*. Its expression is given below.

$$x = \frac{Q^2}{2\nu M_p} \quad (2.7)$$

where $\nu = E - E'$ (the incoming and scattered electron energies) and M_p is the rest mass of the proton. x is the fraction of the proton momentum carried by the struck parton in the collision. It then gives a measure of the density of partons inside the proton, as shown in figure 2.2. The structure functions (see section 2.1) were shown to depend on this ratio.

Also, the inelasticity, y , is a widely used variable in data analysis. It measures the fraction of the incoming electron energy transferred to the proton:

$$y = \frac{p \cdot q}{p \cdot l} \quad (2.8)$$

All these variables can be related by the center-of-mass energy of the collision. The square of the center of mass energy can be defined as follows:

$$s = \frac{Q^2}{xy} \quad (2.9)$$

These variables are important to characterize deep inelastic scattering and are reconstructed using the data as explained in section 4. [10]

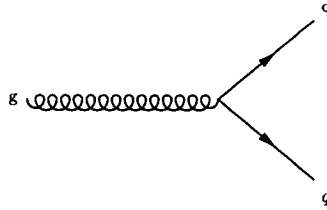


Figure 2.3: A Feynman diagram

2.4 Perturbative QCD

The elaboration of QCD, just like QED, was made on the basis of quantum field theory (QFT), which implies that the interaction is mediated via particles, in this case gauge bosons (gluons in QCD, γ in QED). It is in this context that Richard Feynman came up with a graphical way to express and understand these theories. The method was called Feynman diagram [11], after his work, and an example is shown in figure 2.3. It can be used for all types of interaction. This method made expressions of matrix elements and calculations of cross sections suddenly a lot easier by a set of rules that had to be followed in order to express the matrix elements. The only thing left is to solve them, which is not necessarily an easy problem!

In QFT, when one wants to calculate the cross section of a certain process, one has to consider all possible diagrams that can produce the desired final states. In QED, this is not a problem, since all the higher order diagrams could be easily ignored due to the small coupling constant (higher order diagrams amplitude gets multiplied by the coupling constant in the calculations). In QCD, however, it is more complicated. Divergences can arise from self-interacting loops (e.g. a gluon splitting into a $q\bar{q}$ pair and recombining) when the momentum of the loop goes to infinity (since it does not need to be on the mass shell). These divergencies are called *ultraviolet divergencies*.

Dealing with these divergences arising from QCD is not an easy task. Fortunately, an important feature of QCD, called *renormalization*, can deal with this problem. In this procedure, a cut-off on the loop momentum, called μ_R , is imposed to get rid of the infinities. Consequently, the strong coupling constant acquires a dependence on μ_R , which is an arbitrary parameter and has no physical meaning. It is then important that any physical observable should not depend on μ_R for that precise reason. This is true in an exact calculation, but when an observable is evaluated at a certain order of an approximation, the dependence remains. This is included in the Renormalisation Group Equations. The dependence of α_s on μ_R can be calculated explicitly as a perturbative expansion using the Callan-Symanzik equation (β) as follows.

$$\mu_R^2 \frac{d\alpha_s(\mu_R)}{d\mu_R^2} = \beta(\alpha_s(\mu_R)) = -\beta_0\alpha_s^2(\mu_R) - \beta_1\alpha_s^3(\mu_R) - \dots \quad (2.10)$$

The coefficients β_i in the expansion of equation 2.10 can be found explicitly in [7].

Perturbation theory, which is widely used in QED, cannot be used in the same way in QCD because of the dependence of the strong coupling constant, α_s , on energy, as follows (in the leading order):

$$\begin{aligned}
\alpha_s(Q^2) &= \frac{1}{\beta_0 \ln(Q^2/\Lambda_{QCD}^2)} \\
&= \frac{12\pi}{(33 - 2n_f) \ln(Q^2/\Lambda_{QCD}^2)}
\end{aligned}
\tag{2.11}$$

where n_f is the number of quarks flavours and Λ_{QCD} is a cut-off energy scale (better known as the QCD scale). The value of the cut-off scale is one at which non-perturbative effects start to be important. It has been found to be $\mathcal{O}(200 \text{ MeV})$.

Perturbative QCD is a very useful tool to deal with the interactions at the parton level, where the partons are asymptotically free and the momentum transfer is large. The problems arise when one wants to calculate the contributions to the cross section that come from long-range interactions, where the strong coupling constant is large and pQCD is not valid anymore. However, there exists a useful feature of QCD that allows these calculations to be done.

This feature is called *factorization* and allows us to separate the QCD process in two parts: the long-range and the short-range processes. It comes from the fact that the cross section can be expressed as a hard process (scattering or annihilation of partons) convoluted with the parton distribution functions (PDFs). The latter is a universal function which is process independent. The separation between these two parts is set by an energy scale, called the factorization scale μ_F , but the total cross section should be independent of that parameter:

$$\sigma_{DIS} = \int dx f_p^i(x, \mu_F^2) \otimes \hat{\sigma}^i(x, \mu_F^2)
\tag{2.12}$$

where f_p^i is the PDF of parton i within the proton and $\hat{\sigma}^i$ is the partonic cross section. If the transverse momentum of the parton is less than μ_F , it will get included in the PDF. If not, it is considered in the partonic cross section.

In the fixed perturbation theory approach, one considers the cross section of a process as being made of a series of Feynman diagrams that are classified according to the number of gauge couplings ($g_s = \sqrt{4\pi\alpha_s}$) they contain, or vertices. The simplest group of diagrams adds a contribution to the cross section, which is proportional to the square of the amplitude, of $\mathcal{O}(\alpha_s^n)$, where n is related to the number of vertices. This is called the leading order approximation (LO). Following that logic, the next-to-leading order (NLO) would be $\mathcal{O}(\alpha_s^{n+1})$. The more orders are added to the series, the more accurate the calculation should be. In practice, the series is only asymptotically convergent (i.e. starts to diverge from the true answer after a certain amount of orders).

In this approach, problems can arise in the partonic cross section in the presence of soft partons (with low momentum) or partons that are collinear to their parent parton. These problems take the form of logarithmic divergencies², in addition to the ultraviolet divergencies mentioned previously. A second approach can solve this problem. The original perturbation series for the cross-section in powers of α_s is rearranged in powers of $\alpha_s \ln(Q^2/Q_0^2)$, as shown in equation 2.13, where $L = \ln(Q^2/Q_0^2)$ and Q_0 is an energy cut-off value.

$$d\sigma = \sum_n a_n(\alpha_s L)^n + \alpha_s(Q^2) \sum_n b_n(\alpha_s L)^n + \dots \quad (2.13)$$

The first series in the sum is the *leading logarithm approximation* (LLA), the second term, the *next-to-leading logarithm approximation* (NLLA) and so on, similarly to the fixed-order perturbative approach.

2.5 QCD Improved QPM

The Quark Parton Model, as described in section 2.1, with the help of QCD (described above), had to be modified in order to model nature more accurately. An important point in this modification was the hadron picture of the QPM. A baryon was believed to be made of three point-like quarks. If that was true, the momentum of these three particles should add up to the hadron's

² They are the IR divergencies mentioned earlier in this section.

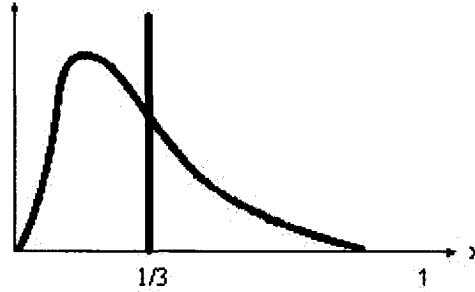


Figure 2.4: *The structure function as a function of the fraction of the hadron momentum carried by the parton, x . If the proton was made of three quarks only, we should observe a solid spike at $x=1/3$ (solid line). If not, then we should see some distribution that is peaked at $x < 1/3$. In this picture, the distribution of three valence quarks tied together with three non-self-interacting gluons is shown.*

momentum. Experiments were made and the results showed that this was not exactly true; the three valence quarks momentum sum was only about half of the total proton's momentum. An example of the evolution of the structure function with x is shown in figure 2.4. So, what was the other half?

The answer came from the gluon, the strong force mediator. The new picture had the proton made of three valence quarks in a sea of gluons splitting into $q\bar{q}$ pairs and recombining. This hypothesis was verified experimentally when the structure function F_2 was shown to have a dependence in Q^2 , which violated Bjorken scaling. For that specific reason, the behavior shown in figure 2.5 is called *scaling violation*.

The structure function F_2 , first defined in equation 2.3, can then be redefined as:

$$F_2(x, Q^2) = x \sum_i e_i^2 f_i(x, Q^2) + x \sum_i e_i^2 \bar{f}_i(x, Q^2) \quad (2.14)$$

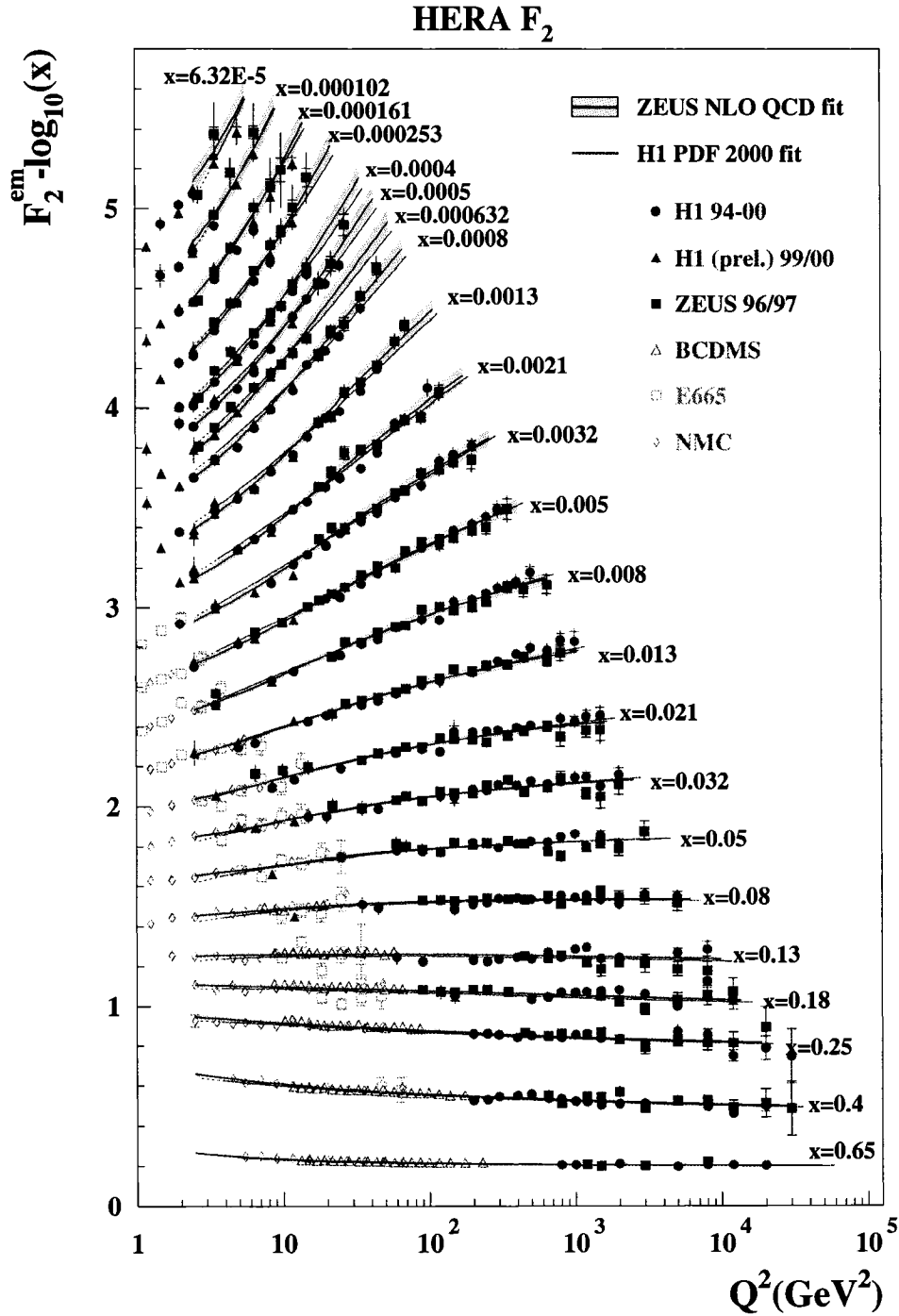


Figure 2.5: *Measurements of the structure function F_2 performed by ZEUS and H1 at HERA, and by other fixed target experiments. At medium values of x ($x=0.08$), Bjorken scaling is observed and scaling violation is shown at extreme values of x .*

The functions $f_i(x, Q^2)$ and $\bar{f}_i(x, Q^2)$ are the quark and gluon density functions inside the proton. They are the parton distribution functions or PDFs and give the probability to find a certain parton (quark or gluon) inside a hadron as a function of x , the fraction of the hadron momentum carried by the parton. The quark PDFs of the proton are separated into sea and valence quarks; valence quarks are the ones carrying the proton's quantum numbers and the sea quarks form the remainder, carrying no net charge since they are originating from gluon splittings. There are different diagrams by which gluons can split: gluon radiation, when a gluon is emitted from a quark, gluon splitting into a $q\bar{q}$ pair and a splitting into 2 gluons (3 gluon vertex) or even 3 gluons (4 gluon vertex). These processes are important since it is through combinations of these that quarks can acquire transverse momentum within the proton.

These gluon splittings, since they change the density of partons inside the proton, have to be included into the PDFs. This is done using the QCD splitting functions for each type of splitting mentioned above. In fact, there are two separate expressions for the parton distribution functions; one involving the quarks, where the gluon radiation splittings is included and another one for the gluons, where gluon-gluon and gluon-quark splittings are taken into account. The amplitude of each of these splittings is described by a splitting function P_{ij} , where i and j are respectively the final parton and initial one. These two separate functions can be obtained by differentiating the PDFs and form a coupled system of differential equations known as the DGLAP equations [12]. They describe the evolution of the PDFs with momentum transfer Q^2 .

$$\frac{dq_i(x, Q^2)}{d\ln Q^2} = \frac{\alpha_s(Q^2)}{2\pi} \int_x^1 \frac{dy}{y} \left(\sum_i q_i(y, Q^2) P_{qq}\left(\frac{x}{y}\right) + g(y, Q^2) P_{qg}\left(\frac{x}{y}\right) \right) \quad (2.15)$$

$$\frac{dg(x, Q^2)}{d\ln Q^2} = \frac{\alpha_s(Q^2)}{2\pi} \int_x^1 \frac{dy}{y} \left(\sum_i g(y, Q^2) P_{gg}\left(\frac{x}{y}\right) + q_i(y, Q^2) P_{gq}\left(\frac{x}{y}\right) \right) \quad (2.16)$$

Since these PDFs cannot be calculated from first principles, an initial scale Q_0^2 has to be input and the DGLAP equations are then used to make them evolve in Q^2 .

The DGLAP equations and their solutions give only the evolution of the PDF in Q^2 , but another evolution scheme exists for the dependence of the PDFs in x . This scheme is called BFKL[13] and it assumes a totally different approach from the DGLAP scheme. After expressing the gluon distribution in a recursive form, one would have to solve the following differential equation.

$$\frac{\partial f(x, k_T^2)}{\partial(1/x)} = \int dk_T'^2 K(k_T, k_T') f(x, k_T'^2) \quad (2.17)$$

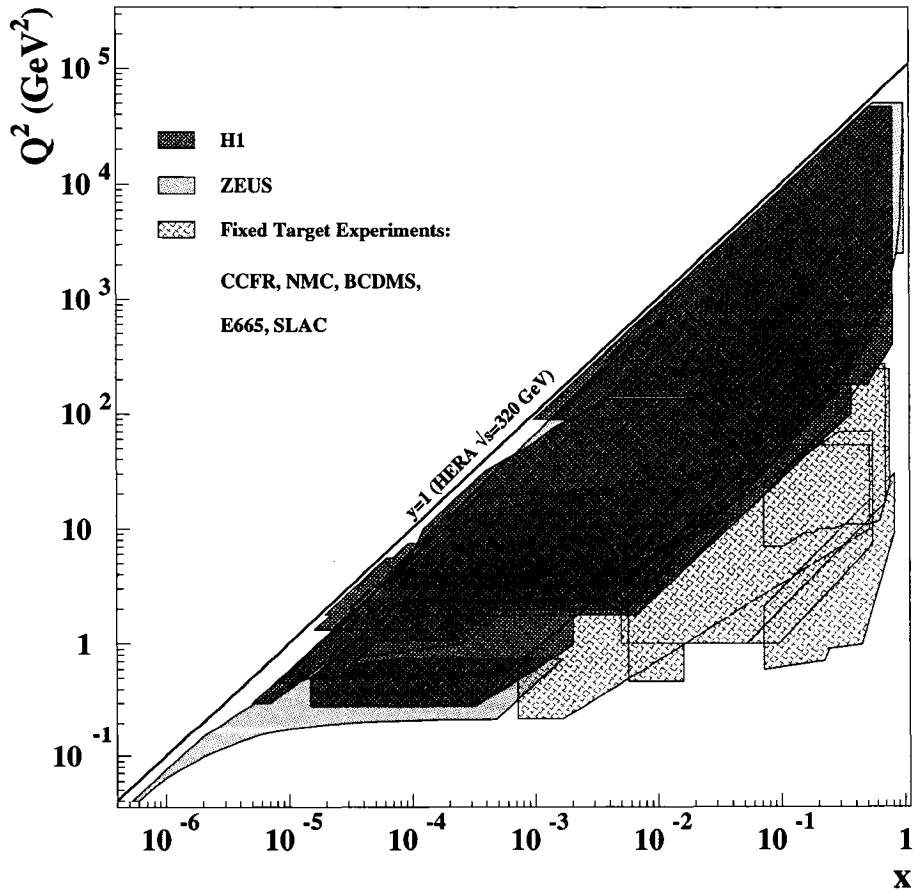


Figure 2.6: Kinematic region covered by the HERA experiments, ZEUS and H1.

$K(k_T, k'_T)$ is the BFKL kernel, $f(x, k_T^2)$ is the gluon distribution and k_T is the transverse momentum of the emitted partons. When solved for a fixed α_s , this evolution scheme is very interesting since it also fits the F_2 structure function measurements as a function of x obtained at HERA. [14]

2.6 Deep Inelastic Scattering

Before HERA, the confirmation for perturbative QCD mostly came from fixed target experiments. With the construction of HERA at the end of the 1980's, scattering experiments were brought to new limits. HERA was the first collider to study deep inelastic scattering with a center-of-mass energy \sqrt{s} of 300(318) GeV (see section 3 for more details). It was even called a “QCD factory” due to its coverage of a whole new area of the (x, Q^2) as shown in figure 2.6.

In lepton-nucleon scattering, since the two colliding particles are of different sizes, the lepton can have up to 50 TeV in the proton system and can be used as a probe to “see” inside the proton. The lepton, with sufficient energy, will interact directly with a particular parton inside the proton. In order to do this, the energy transferred between the lepton and the nucleon has to be above a threshold. This kinematic regime is called *Deep Inelastic Scattering* (DIS) and allows to study the substructure of the proton; “deep” because of the great momentum transfer and “inelastic” because the proton is “broken” in the process.

Scattering processes at an ep collider have to proceed via the exchange of a gauge boson (as required by quantum field theory). At lowest order, two main types of Feynman diagrams describe that type of electroweak interaction. They are shown in figure 2.7. When the exchanged boson is a photon or a Z^0 , both neutral, we talk about neutral current (NC), since the lepton type and charge are unchanged. In the case of a W^\pm exchange, the boson is charged, hence the name charged current (CC). In this case the scattered lepton is a neutrino.

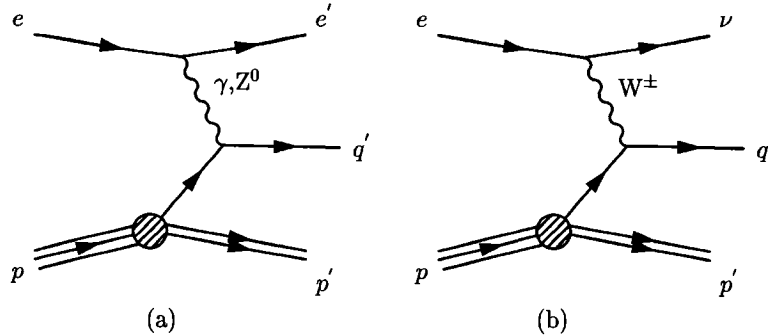


Figure 2.7: *Feynman diagrams for DIS: (a) lowest order NC and (b) lowest order CC*

In the present analysis, we concentrate on NC events, since we use the detection of the electron as a tool to tag events and also because of high statistics. In the CC events, the neutrino cannot be detected directly, but rather inferred from the missing momentum.

2.7 Resonance Production

With these building blocks in hand (quarks and gluons), it is then possible to form a wide variety of hadrons. Most of them are relatively stable, meaning that they live long enough for their passage to be measured in the detector. They are called *long-lived particles*.

There exist also a number of hadrons that have a very short lifetime, hence their name, *short-lived particles*. These particles can only be observed through their decay products, which are stable enough to be detected. They are also known as *resonances*. This word was used in the first place because these particles were showing up as resonances or peaks in the mass (energy) spectrum of detected signals, without being seen. With the advances of technology, many resonances can now be seen in tracking detectors.

In order to measure a resonance signal, a favorable decay channel has to be chosen (high branching ratio and stable decay products) and the invariant mass spectrum of the products has to be measured. This analysis covers the

production of three particles, which have a common decay channel, ρ^0 , $f_0(980)$ and $f_2(1270)$. The $\pi^-\pi^+$ decay channel which is the most abundant for all three will be studied.

The ρ^0 meson is a light meson, i.e. made of u and d quarks as valence quarks. It is a vector meson, meaning that it has an intrinsic angular momentum $J^P = 1^-$. This comes from the fact that the quark and anti-quark in the ρ^0 meson have their spins aligned (quarks are fermions with $\frac{1}{2}$ -spin). It can be considered as an excited state of the pion, or π meson, which has the same quark content, but an angular momentum $J^P = 0^-$. This explains the higher mass of the ρ^0 meson for the same quark content, since an aligned spin-state contains higher energy.

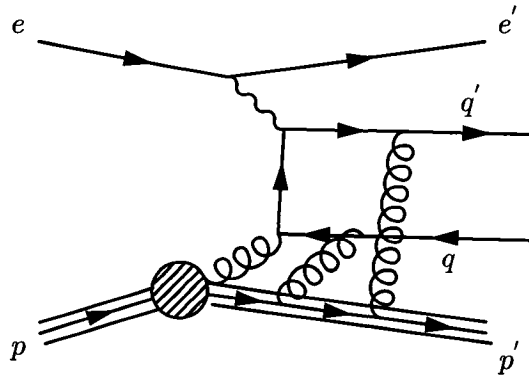


Figure 2.8: Feynman diagram for ρ^0 production

The quark content of the ρ^0 , according to pQCD, can come from the following production mechanism [15]: after the hard scattering, an interaction would occur between the proton remnant (the partons from the proton which did not interact in the collision) and the $q\bar{q}$ pair via gluon radiation as shown in figure 2.8. The quarks would then fluctuate and recombine later on to give rise to the ρ^0 meson. This hypothesis could also be applied to the f resonances but further studies would be needed.

The f resonances are made of a linear combination of $u\bar{u}$, $d\bar{d}$ and $s\bar{s}$ pairs. f_0 and f_2 have different intrinsic angular momentum, respectively 0 and 2 for f_0 , and f_2 , which makes them scalar and tensor mesons, respectively [16]. Following the previous logic, the angular momentum J of the f resonances comes from the alignment of the different $q\bar{q}$ pair in the linear combination which forms them.

2.8 From Theory to Experiment

In order to measure the cross section of these three resonances, the invariant mass of $\pi^-\pi^+$ will be measured and fitted. It has already been done in H1 in the photoproduction regime [17] and it is of interest for ZEUS to measure it at the center-of-mass energy of HERA in DIS. It will help our understanding of the inclusive cross section at HERA.

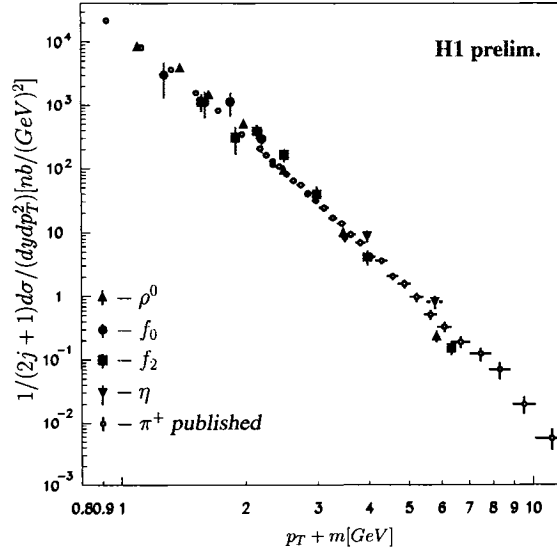


Figure 2.9: H1 results for double differential cross sections of η , ρ^0 , f_0 and f_2 mesons compared with previous results for pions. [17]

This experiment also has an important theoretical implication. The measurement of the f_2 meson cross section can be used to verify the existence of the odderon in the production mechanism of this meson. The odderon is an effective object which can be exchanged in high-energy reactions and that is

pictured as a three-gluon exchange. Previous data from the E687 experiment at Fermilab have not ruled out the possibility for an odderon exchange, without getting a number for the cross section since they did not have enough statistics. A measurement of the cross section by a HERA experiment could shed light on this tensor meson production and on the existence of the odderon [18].

It can also be shown, using the cross section measurements, that there is a universality between long-lived and short-lived hadrons, or resonances. This was done by the H1 collaboration [17] and their results are shown in figure 2.9. The pions, which are stable mesons, are compared here with the three mesons studied in this thesis and the η meson.

3 ZEUS: A Detector for HERA

The present analysis was performed using ep collisions at the HERA accelerator. The data was obtained with the ZEUS detector, located at DESY (Deutsches Elektronen Synchrotron) in Hamburg, Germany. The accelerator and the components of the detector used in this analysis are discussed below. A complete description of the ZEUS detector can be found elsewhere [19].

3.1 HERA: die “Hadron Elektron Ring Anlage”

The Hadron Electron Ring Accelerator (HERA) [20] is the first lepton-proton collider in the world. It has a circumference of 6.3 km and is located 15-25 m underground. It consists of a tunnel where the particles are circulating and four halls which contain the HERA experiments: ZEUS, H1, HERMES and HERA-B. The four halls are completely underground, with only small accesses at the ground level. The tunnel contains two separate rings, one for the leptons and the other for the protons. At two points in their trajectory, the rings meet to allow collisions to happen. These two points are located in the North hall for H1 and in the South hall for ZEUS. The two other experiments are fixed-target experiments; HERMES studies the spin structure of the nucleon and HERA-B³ tried to measure CP-violation in decays of B mesons into the so-called “golden decay mode”.

Different injection and acceleration systems are used for each type of particle as can be seen in figure 3.1. The electrons are produced and preaccelerated in a linear accelerator, LINAC I, until they reach 220 MeV. In the case of positrons, the particles, produced by bombarding electrons on a tungsten target [21], are preaccelerated by LINAC II up to 450 MeV and then stored in the positron intensity accumulator (PIA). The leptons are then transferred to the DESY II synchrotron, where they are accelerated to 7.5 GeV and sent to PETRA. When they reach 14 GeV, they are finally injected into HERA in up to 210 bunches of $\mathcal{O}(10^{10})$ particles with a 96 ns bunch crossing interval. The electron⁴ magnet system in HERA is made out of normal conductor dipoles

³ The HERA-B experiment stopped its activities in February 2003.

⁴ The term “electron” is used to refer to both electron and positron throughout this thesis.

operating at room temperature to bend the electrons trajectory using a field of 0.16 T. Quadrupole and sextupole magnets are also used for focusing and for trajectory correction of the beam. RF cavities, operated at a frequency of 500 MHz, are used to accelerate the electrons throughout the whole accelerating system to their nominal energy of 27.5 GeV.

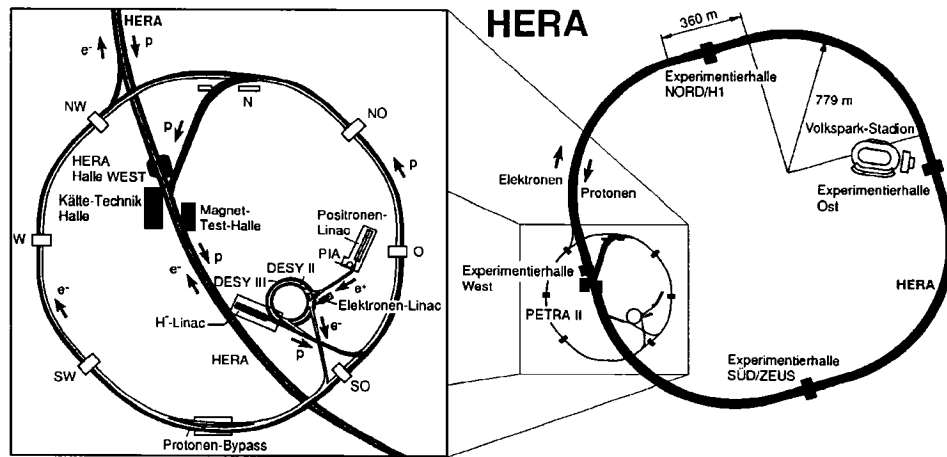


Figure 3.1: Overview of the HERA accelerator with a close-up view of the preacceleration system

For the protons, the injection starts with H^- ions which are directed into the 50 MeV Proton Linac. From there, the protons are fed into the proton synchrotron, DESY III, for them to reach 7.5 GeV. They are then transferred to PETRA, for the last preaccelerating stage up to 40 GeV and finally, they are injected into HERA. Starting in 1998, the nominal proton energy was 920 GeV, which was an upgrade from the original nominal energy of 820 GeV, and thus increasing the center-of-mass energy from 300 to 318 GeV. In order to reach that energy, RF cavities are used with different frequencies in each accelerating machine. Superconducting magnets, operating at 4.4 K, are used to bend the beam with a 4.7 T magnetic field. In order to keep the magnets at this temperature, liquid helium is circulating around the ring and is kept at constant temperature by four refrigerating units located in the four halls.

3.2 The ZEUS Detector

The ZEUS detector is located in the South Hall of HERA. It is a general purpose particle detector designed to measure the different aspects of ep scattering. This particularity requires an asymmetry in the construction of the detector, between the forward and the rear region, caused by the difference in energy between the incoming proton and lepton. This creates a system where the center-of-mass frame moves in the direction of the proton beam with respect to the laboratory frame. An overview of the detector is shown in figure 3.2.

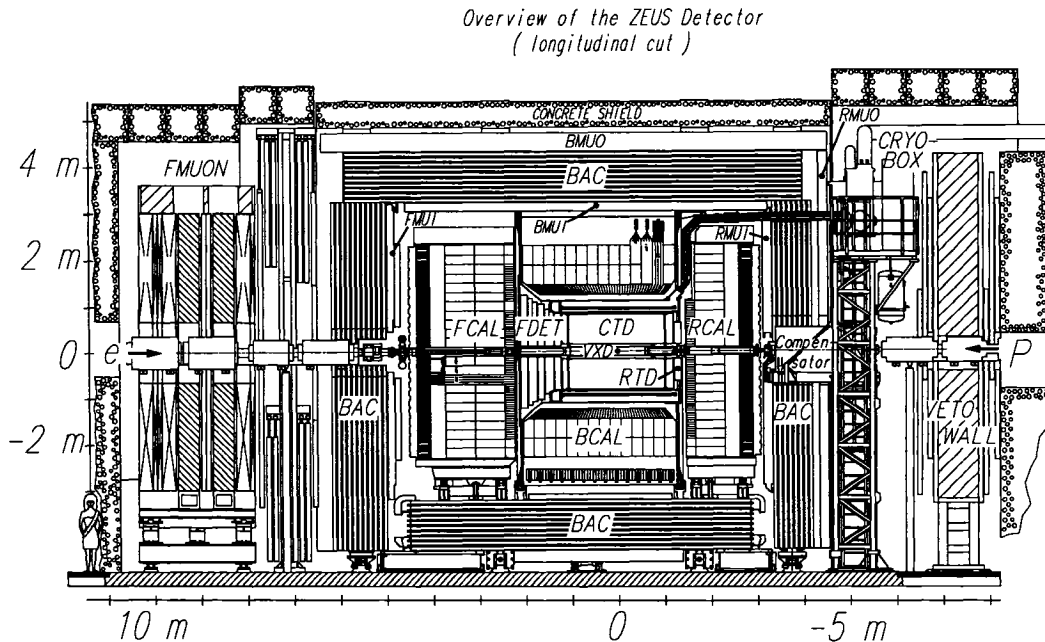


Figure 3.2: Overview of the ZEUS detector as of 1993. The incoming electron comes from the left and the incoming proton, from the right. See text for abbreviation details.

The coordinate system is a right-handed system, where the positive z -axis is in the direction of the proton thus defining the forward region, the rear region being in the direction of the incoming lepton. The origin is located at the nominal interaction point (IP) and the spherical polar angles, polar (θ) and azimuthal (ϕ), are defined. The pseudorapidity η , defined as $\eta = -\ln(\tan(\theta/2))$, is more commonly used instead of θ since it is Lorentz invariant.

During the data taking period 1998-2000, no inner vertex detector was installed; the previous VXD was removed in the 1995-1996 shutdown and the MVD (Micro Vertex Detector) was installed in the 2000-2001 shutdown. The tracking part of the detector is mainly composed of the CTD (Central Tracking Detector), which is a drift chamber, as described in section 3.2.1. The tracking system is completed by the FDET (Forward Detector), composed of the FTD (Forward Tracking Device) and the TRD in the forward region and of the RTD (Rear Tracking Device) in the rear region. The F/RTD are planar drift chambers designed to measure the low/high angle tracks with better efficiency and the TRD (Transition Radiation Detector) serves as an electron/hadron separator in the forward tracking region. In the rear region, a small rear angle tracking detector (SRTD) improves the θ -coverage in front of the calorimeter. This whole system allows for a precise measurement of the momentum of charged tracks and thus the reconstruction of event and decay vertices. The chambers are surrounded by a superconducting solenoid, producing an axial magnetic field of 1.43 T necessary for the tracking measurements. A background radiation detector, the C5 counter, is placed in the central cutout of the RTD around the beam pipe, at 1.2 m from the nominal interaction point. It is made of scintillator plates interleaved with tungsten layers.

The detector is completed by an uranium calorimeter, as described in section 3.2.3, which measures energy deposition from outgoing particles and by an iron yoke. Inside this yoke, a backing calorimeter (BAC) is installed. On each side of the BAC, muon detectors are installed, namely FMUI, BMUI and RMUI inside and FMUON, BMUON and RMUON outside the BAC. Behind the rear calorimeter, at 7.5 m from the interaction point, a VETO wall, made of an iron wall covered with scintillator hodoscopes, is used to protect the detector against the proton beam halo background. The detector is finally coated in a concrete shielding and the acquisition electronics is located partly on the detector and partly in the "Rucksack", a three stories high building next to the detector in the Hall.

3.2.1 The Central Tracking Detector (CTD)

The Central Tracking Detector, as the main component of the tracking system, provides a precise measurement of the momentum of charged particles. It can also be used for particle identification purposes, using the dE/dx energy loss measurement performed inside the gas-chamber volume.

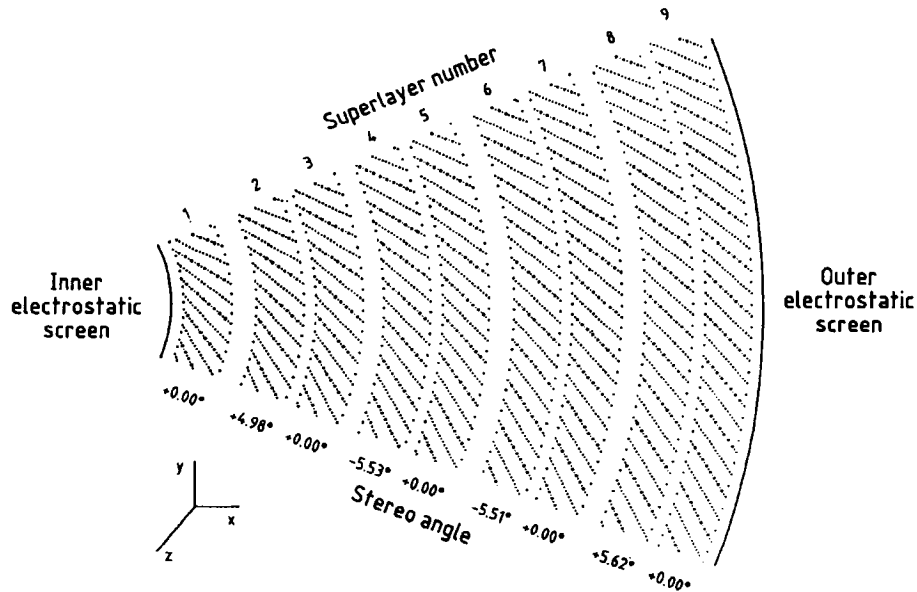


Figure 3.3: View of the wire layout of an octant in the Central Tracking Detector

It is a cylindrical wire chamber [22] made of nine superlayers (SL). Each of these superlayers is divided into cells of eight sense wires. The number of cells increases with radius from 32 cells for SL1 to 96 cells for SL9, for a total of 576 cells as shown in figure 3.3. In order to allow z determination which provides a good polar angle accuracy, four superlayers (even-numbered) out of nine have a stereo angle; the other five (odd-numbered) have their sense wires parallel to the beampipe. The stereo angle is kept small ($\pm 5^\circ$) to ensure that the angular resolution in both polar and azimuthal angles is roughly equal. A z -by-timing system has also been implemented on SL1, 3 and 5 to evaluate the z -vertex at a faster rate for trigger decisions. The 4608 sense wires that constitute the chamber are included in an active volume of 203 cm in length,

with an inner radius of 18.2 cm and an outer radius of 79.4 cm. This allows for a polar angle coverage of $15^\circ < \theta < 164^\circ$ (provided there are hits in at least 12 sense wire layers) and a full azimuthal angle (ϕ) coverage.

When charged particles enter the CTD, they ionize the atoms of the gas⁵ along their path, creating free electrons. These electrons will then drift along the electric field to the sense wires with a constant drift velocity of $50 \mu\text{m}/\text{ns}$, where they will create an avalanche (multiplication of the number of electrons by a factor of 10^4) under the action of the strong electric field. The measurable signal produced is then sent every 9.6 ns to the flash analog to digital converters (FADC) for data acquisition [23].

3.2.2 Vertex and Track Reconstruction

The particle tracks and vertices are obtained by the track finding algorithm VCTRAK [24]. This package uses the raw data information, stored in ADAMO [25] tables, to fill output tables of fit parameters for physics analysis purposes. A track candidate begins with a 3-point seed located in an outer axial superlayer of the CTD. The arc in the r - ϕ plane is then extrapolated inward through the magnetic field, gathering more hits on its way toward the inner superlayers. It is then used for stereo and z-by-timing pattern recognition that superimposes the stereo hits to the arc. Tracks with too many shared hits are discarded. The longest tracks are found first, then the shorter ones, up to the shortest ones, with hits only in SL1.

The track candidates are then fitted to a 5-parameter helix model. The fit parameters are stored in the VCTRHL⁶ table. A three-stage primary vertex finding algorithm [26] is then applied. First, a filtering of incompatible trajectories is done, then a vertex “simple fit” is applied to get a starting point for the last stage, the full fit. In this last step, tracks associated with the primary vertex are refitted and stored in the VCTPAR table. For this analysis, only tracks from VCTPAR table have been used.

⁵ A gas mixture of argon, CO_2 and ethane (C_2H_6) bubbled through 0.84% ethanol in the proportion 83:5:12 is used. It is preferred to a 50:50 argon/ethane mix for safety reason and to avoid whisker growth on wires.

⁶ VCTRHL and VCTPAR tables are part of the VCTRAK package.

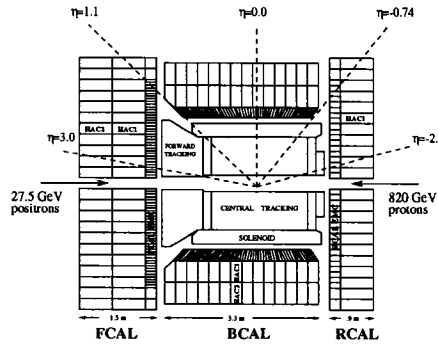


Figure 3.4: Overview of the Calorimeter

3.2.3 The Uranium Calorimeter (CAL)

The energy deposited by the particles leaving the tracking system is measured by the Calorimeter [27]. In order to achieve this, the ZEUS experiment uses a sampling calorimeter with depleted uranium (DU)⁷ as absorber material and an optical readout system based on scintillator tiles as detector medium. 3.3 mm-thick DU plates clad in stainless steel foil are interleaved with 2.6 mm-thick SCSN-38 tiles, a cast polystyrene material. Uranium offers many advantages over other absorbers. First, it has a heavy and dense nucleus, allowing for more interactions with the incoming particles, thus keeping the calorimeter compact. Moreover, the natural radioactivity of the uranium provides a stable signal for calibration within 1% accuracy. The use of DU also allows to adjust the response of both parts of the calorimeter, electromagnetic and hadronic. An enhancement of the hadronic response and a suppression of the electromagnetic one is done, leading to a compensating calorimeter, where $e/h = 1$ (e being the electromagnetic response and h , the hadronic response). Compensation ensures the best energy resolution for hadronic showers.

The high resolution calorimeter has a modular structure and is divided into three sections: barrel, forward and rear as can be seen in figure 3.4. With this structure, it can cover 99.8 % of the solid angle in the forward region and 99.5 % in the rear. The barrel calorimeter (BCAL) is subdivided azimuthally in 32 wedge-shaped modules and longitudinally in 14 towers. It covers the interaction region and the CTD. Every tower has 4 electromagnetic (EMC)

⁷ Depleted uranium is made of 98.1% ²³⁸U, 1.7% Nb and less than 0.2% ²³⁵U.

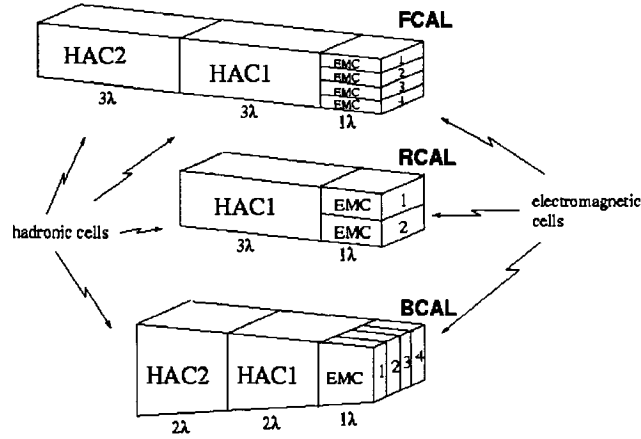


Figure 3.5: *Cell layout in the three sections of the Calorimeter*

cells and 2 hadronic (HAC) cells, as shown in figure 3.5. Each cell is read out by 2 photomultiplier tubes (PMT) for redundancy in case of failures and for better lateral position measurement accuracy. The light is sent from the scintillators to the wavelength shifters and then to the PMTs. The signal is then sent to the electronics, where pulse height and arrival time are measured, in order to reconstruct energy and timing information. The EMC sections are $25 X_0$ (radiation lengths) deep and the HAC section, $52 X_0$, for a total of 5λ (interaction lengths).

The forward (FCAL) and rear (RCAL) calorimeters are shaped as planar disks and subdivided vertically into 23 modules and horizontally into 23 towers, not all of them having the same cell composition. For FCAL, the cells located outside the shadow of BCAL contain 4 EMC and 2 HAC cells per tower. In the outer ring, the EMC cells are replaced by hadronic (HAC0) cells. A similar pattern is used in RCAL, except that the thickness is reduced; only 2 EMC cells and 1 HAC cell are necessary there. Also, the asymmetry between these calorimeters is visible in the thickness of the segments: 21 and $25 X_0$ for EMC and 42 and $85 X_0$ for HAC for a total of 7 and 4λ , for RCAL and FCAL respectively. The cell layout for each section of the CAL is detailed in figure 3.5.

With such a configuration, the calorimeter can achieve a high energy resolution. For electrons, the resolution is $18\%/\sqrt{E}$ and for hadrons, $35\%/\sqrt{E}$ (E in GeV) as measured in test beam conditions. The electromagnetic resolution is not particularly high but quite acceptable, while the hadronic resolution is very good.

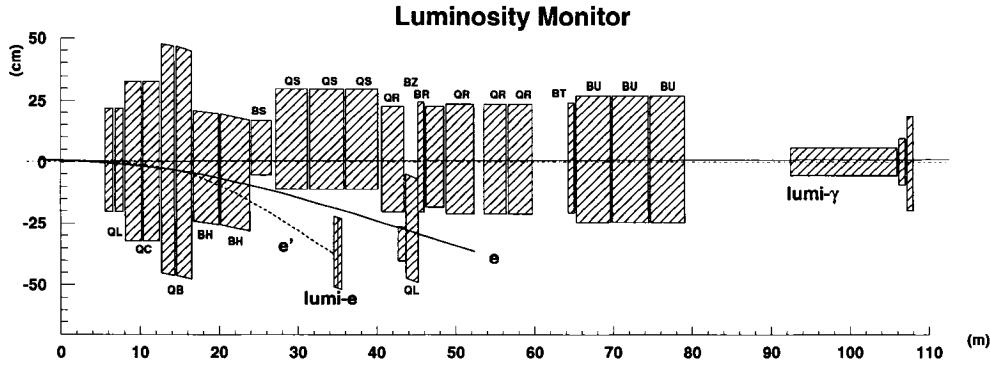


Figure 3.6: The Luminosity Monitor

3.2.4 The Luminosity Monitor

In order to extract the cross section of a certain process, one needs the luminosity measurement. The luminosity is a quantity which weights the cross section to ensure the universality of its measurement. To do this, the LUMI [28] detector uses the Bethe-Heitler process [29], $ep \rightarrow ep\gamma$, for which the cross section is well known, within small radiative corrections. Using the following definition of the luminosity, $\mathcal{L} = R/\sigma$, where R is the rate of events for a certain process and σ is the cross section of the same process, one can extract the luminosity by measuring the rate of events.

The LUMI system is made of two separate detectors, a photon and an electron detector (see figure 3.6). The photon detector is a calorimeter located 104 m away from the interaction point. It is a lead/scintillator sandwich calorimeter protected from synchrotron radiation background by a carbon filter and combined with a Cherenkov counter. The electron detector is located at 35 m from the interaction point and uses the same type of calorimeter, without

filter. Both calorimeters have an energy resolution of $18\%/\sqrt{E}$, but the carbon filter of the γ -detector worsens this value by only a few percents. The LUMI detector gives a measurement accurate within 2.25% for the 1998-2000 running period.

Background arising from beam gas interactions (electron bremsstrahlung) is subtracted using the unpaired bunches from the beam. Some electron bunches do not have a corresponding proton bunch to collide with and electron bremsstrahlung can be measured from these and removed from the luminosity measurement. The electron detector can also be used to tag photoproduction events, where the electron is detected at a very small angle.

3.3 Data Acquisition and Trigger

During data taking, HERA is delivering collisions with a bunch crossing interval of 96 ns. This creates a high rate of events for the DAQ chain to cope with, namely 10.4 MHz. On the other hand, not all such events are relevant; in fact, a lot of background caused by beam gas interaction and cosemics have to be discarded in order to keep only the relevant physics events (~ 10 Hz) for analysis. In order to solve this problem, ZEUS is using a three-level trigger chain. A schematic view of the trigger chain is shown in figure 3.7. [30]

The First Level Trigger (FLT) is a hardware-based system. Every component has a subtrigger which uses pipelines, clocked by the 96 ns bunch crossing interval, to allow the calculations to be performed. All the subtriggers are then directed to the Global First Level Trigger (GFLT) which synchronizes this data with the bunch crossing number. It has $4.4 \mu\text{s}$ (or 46 bunch crossings) to make a decision before the data is sent for digitization. During normal operation, the GFLT is expected to be almost deadtimeless. Using calorimeter information, the Fast Clear (FC) can be used to abort background events before they reach digitization.

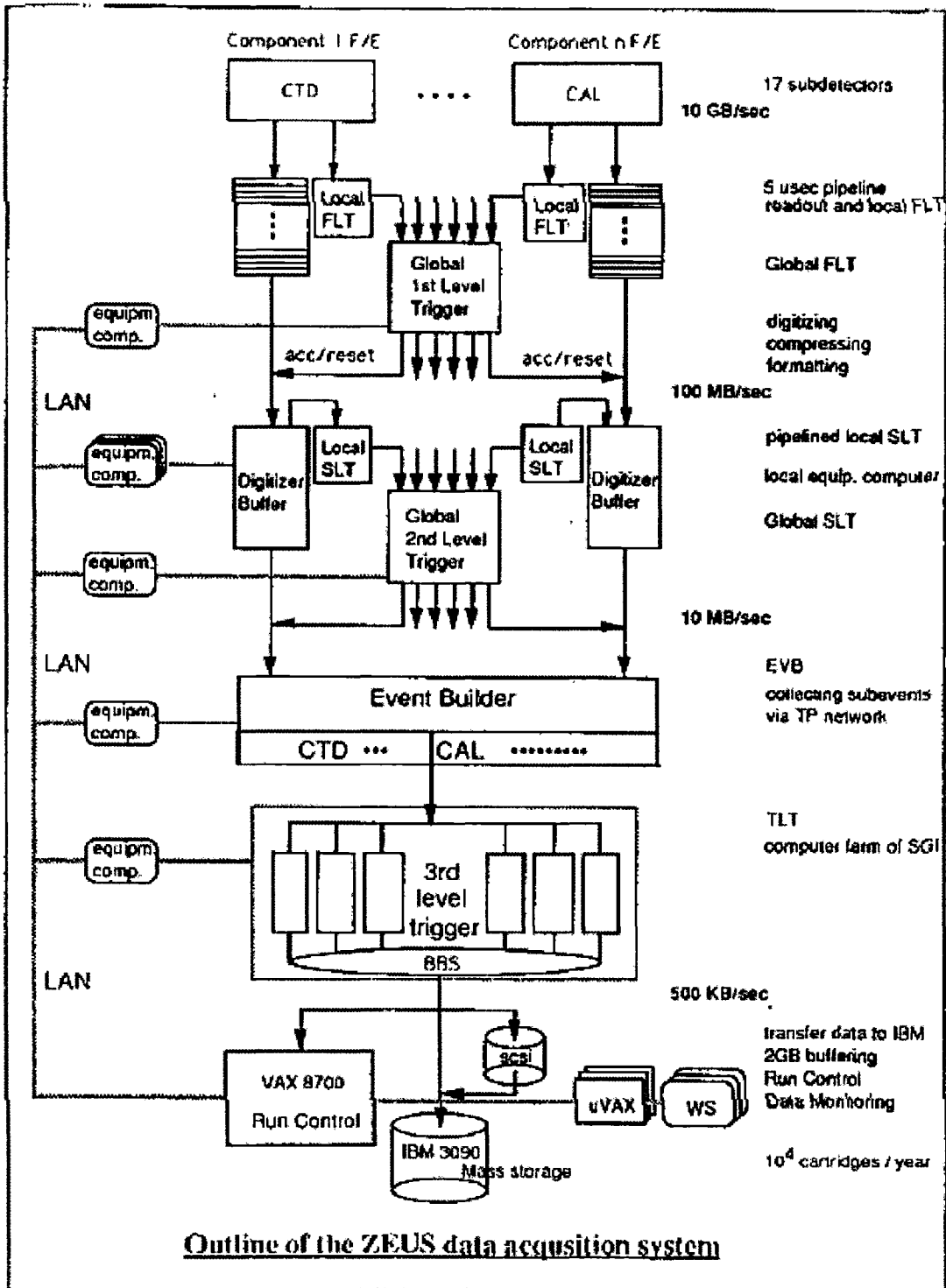


Figure 3.7: The ZEUS trigger chain

The Second Level Trigger makes use of the digitized data produced after an accept from the FLT to make a decision. The aim is to reduce the rate by a factor of 10, from ~ 1 kHz to ~ 100 Hz. It makes an extensive use of transputers to process vertex, momentum, cluster energy and timing information in parallel [31]. Like the FLT, it is made of component subtriggers which are sent to the Global Second Level Trigger. The GSLT accept is then sent to the components using the Event Builder (EVB), which collects data from all components.

The EVB is also used to transfer the information into a suitable format for analysis and reconstruction: the ADAMO tables. These are then sent to the Third Level Trigger (TLT), which was a SGI-computer⁸ farm designed to reduce the rate to 10 Hz using offline filter code. Accepted events are sent to Data Summary Tapes (DST) which are then used for analysis. The TLT classifies the events into trigger bits, which are used to select events. For this particular analysis, the trigger chain used will be described in section 4.

⁸ It is now composed of PCs since the 2000 upgrade.

4 Event Selection

The ZEUS detector is designed to record a lot of different types of events. The trigger system (see section 3.3), apart from discriminating interesting physics from background, has also the task of classifying the events according to certain requirements. The requirements are mainly upper or lower limits on physical quantities such as energy deposited, position, momentum, etc. According to these cuts, the events will be tagged *online* by a trigger bit which allows an easier selection of events for physics analyses and an efficient rejection of the background.

Trigger bits are usually designed for known or very frequent processes, like charm production or hard photoproduction. For this analysis, no specific trigger for vector mesons exists and the combination of triggers had to be as inclusive as possible, without allowing too much background. The events written on tape are then used for the *offline* selection, which is a code-based set of cuts allowing to choose only the relevant events for the analysis.

In order to obtain the cross section measurements with the ZEUS detector, two types of events are needed: the real physics events and the simulated events, described in section 5. The production and analysis of these events has to be similar, as shown in figure 4.1, to allow comparison between them. The event selection described below was applied to both types.

4.1 Online Event Selection

The online event selection is done during data taking. Every trigger level increases the accuracy of the decision, because of the greater amount of information and time available for computations. The cuts then become tighter with the increasing trigger level.

In order to select neutral current DIS events, the scattered electron is required to be detected with a calorimeter energy greater than 4 GeV. For the process $V \rightarrow \pi^\pm \pi^\mp$, where V is one of the three studied mesons, namely ρ^0 , f_0 and f_2 , a logical OR of the TLT filters DIS01 and DIS03 was used. DIS01

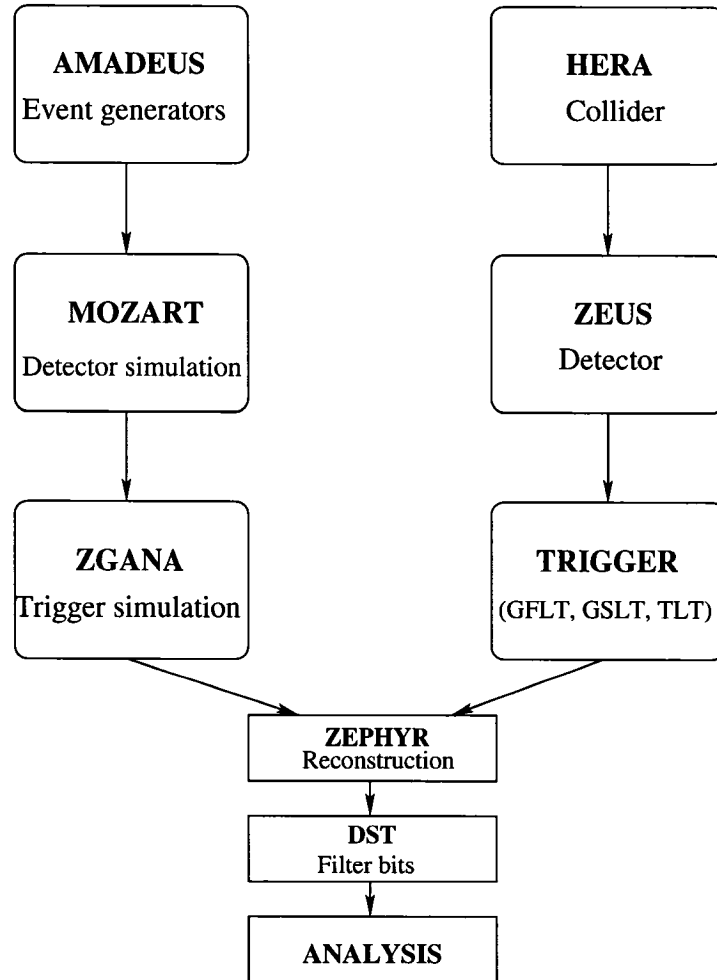


Figure 4.1: *The event production and analysis chain for data (right) and simulated events (left). Both types of event produce the same output format to be used in the analysis step.*

is a fully inclusive prescaled low Q^2 trigger. Prescaling means that not every event which passes successfully the trigger selection is taken, but only one every n events, where n is the prescale factor. This has to be done in order to reduce deadtime. DIS03 is an inclusive medium Q^2 trigger (not prescaled). This combination of filters then allows a larger selection of low Q^2 DIS events. Each of these filters is made of a combination of different FLT and SLT slots (at least one of them at each level has to be taken) and a software-based TLT decision is taken from them [32].

4.1.1 First Level Trigger

At the FLT level, decisions have to be taken quickly with a reduced amount of information from the Calorimeter and CTD First Level Triggers, for energy and tracking information. Energy information consists of energy sums or isolated energy deposit (IsoE) from the CAL. A “good track” requirement is used from the CTD, which is a track coming from the nominal interaction region, $-50 \text{ cm} < z_{\text{vertex}} < 80 \text{ cm}$. For DIS03 and DIS01, the chain FLT40.OR.FLT41.OR.FLT42.OR.FLT43.OR.FLT44.OR.FLT46 is used. The FLT slots are described below.

- FLT40: TRUE if $E^{EMC} > 15 \text{ GeV}$
- FLT41: TRUE if $E_T^{CAL} > 21 \text{ GeV}$
- FLT42: TRUE if there is one good track .AND. ($E^{CAL} > 15 \text{ GeV}$.OR. $E^{EMC} > 10 \text{ GeV}$.OR. $E^{BEMC} > 3.4 \text{ GeV}$.OR. $E^{REMC} > 2 \text{ GeV}$)
- FLT43: TRUE if there is one good track .AND. $E_T^{CAL} > 11.5 \text{ GeV}$
- FLT44: TRUE if $E^{REMC} > 3.4 \text{ GeV}$.OR. $E^{BEMC} > 4.8 \text{ GeV}$
- FLT46: TRUE if $\text{IsoE}^{RCAL} > 0 \text{ GeV}$.AND. ($E^{REMC} > 2 \text{ GeV}$.OR. (there is a good track .AND. there is SRTD data) .OR. (there is a good track .AND. $E_T^{CAL} > 18 \text{ GeV}$))

In addition to these, timing information from the Veto Wall, C5 counters and SRTD is needed to reject background coming from beam-gas interactions or cosmics events. Since the events originating from non-physics events have a time stamp different from 0 ns ($t = 0 \text{ ns}$ is the time associated with the interaction point), they can be rejected immediately with high efficiency.

4.1.2 Second Level Trigger

The SLT uses information from all components and more precise information from the already used components, namely CAL and CTD. For the selection of DIS events using the CAL, an important quantity is $E - p_z$. For the incoming proton, $(E - p_z)_p = 920 - 920 = 0 \text{ GeV}$ since it goes in the positive z direction.

On the other hand, the incoming electron has $(E - p_z)_e = 27.5 - (-27.5) = 55$ GeV. Since we require the electron to be detected inside the calorimeter, using momentum conservation, a DIS event must have $(E - p_z)_{CAL} \sim 55$ GeV. In the case of Initial State Radiation (ISR) from the electron, a photon is emitted before the collision in the rear beam pipe and has to be considered in the calculation. Therefore, the energy from the LUMI E_γ^{lumi} is included.

SLT also uses the CTD z-by-timing information (see section 3.2.1) to determine the z-position of the primary vertex within accepted limits for the interaction region. This adds to the FLT timing information to reject background events not coming from the interaction point.

For DIS01 and DIS03 filters, one SLT slot is used, DIS6, which is described as:

TRUE if $E - p_z + 2 \cdot E_\gamma^{lumi} > 29$ GeV .AND. ($E^{REMC} > 2.5$ GeV .OR. $E^{BEMC} > 2.5$ GeV .OR. $E^{FEMC} > 10$ GeV .OR. $E^{FHAC} > 10$ GeV)

4.1.3 Third Level Trigger

The software-based TLT has all the information from the detector and more time than the two other levels. It can then use information like the RCAL position or the completely reconstructed event vertex from the CTD. An improved measurement of $E - p_z$ is also included. It is at the TLT level that DIS01 and DIS03 triggers are differentiated from each other.

The two filters are described as follows.

- DIS01: TRUE if $E_e^{CAL} > 4$ GeV outside a box of 24x12 cm² in RCAL around the beam pipe hence accepting low Q² events. It can take different prescale factors, depending on the trigger configuration.
- DIS03: TRUE if $E_e^{CAL} > 4$ GeV outside a radius of 35 cm in RCAL around the beam hence accepting medium Q² events.

The Q² selection is done by the box/radius cut, so it is impossible to know the precise Q² cut between DIS01 and DIS03. The closer the electron is to the

Year	Run Ranges	DIS01		DIS03	
		Prescale	Luminosity (nb ⁻¹)	Radius cut (cm)	Luminosity (nb ⁻¹)
1998 e ⁻	30758 - 31544	100	31.363	R > 25	4610.111
	31557 - 31752	1	1473.810	R > 25	
1999 e ⁺	31784 - 32213	1	3220.840	R > 25	12101.533
	32214 - 32906	100	88.778	R > 25	
1999 e ⁻	33125 - 34486	10	1962.447	R > 35	19624.475
2000 e ⁺	35031 - 37584	10	4469.674	R > 35	12262.712
	37646 - 37715	10	98.927	R > 35	

Table 4.1: TLT prescale and cuts over the year 98-00 [33]

beampipe in RCAL, the lower Q^2 is. A good estimate is that DIS01 accepts events with $Q^2 \gtrsim 2 \text{ GeV}^2$ and DIS03, with $Q^2 \gtrsim 25 \text{ GeV}^2$. More details about the prescale factors and the box/radius cut can be found in table 4.1.

After the TLT decision, the data is stored on tape and later sent to the offline reconstruction package, ZEPHYR (ZEus PHYSics Reconstruction). It makes use of the data of each component and the associated calibration to obtain tracks, clusters and energy flow objects (EFOs) hence combining the information for the different parts of the detector. It then writes the output to Data Summary Tapes (DSTs). Each DST contains a particular selection of events using yet another filter that can be accessed using the DST bits. For this analysis, DST9 was used which is a common DIS bit that requires at least one of the 4 predefined electron finders to find an electron with $E_e > 4 \text{ GeV}$. Since the DST bits are set at reconstruction time with all the information available for the event, the selection might differ from the trigger [34].

4.2 Offline Event Selection

In order to tighten the requirements made at the trigger level, to reject residual background and also to select very specific events, other event selections are made *offline*. This time, all the information is available to reconstruct the event and processing time is not limited. The offline selection is software-based. Using these criteria, a selection of 2 680 920 events out of a 82.5 nb^{-1} sample was made.

4.2.1 Calorimeter Noise and ‘Sparks’ Suppression

The calorimeter PMTs on the detector side can also be a source of background. They can be noisy (then included into the bad channel list during daily CAL calibration) or they can produce sparks. A spark happens when an electric discharge occurs between the cathode and the shielding of the PMT. If that happens in the electromagnetic section, it can be wrongly tagged as an electron deposition for trigger decision. The imbalance of the signal between the redundant PMTs for the cell is then used to detect and suppress this noise by keeping only the measurement from the smallest signal of the two PMTs and applying it to both sides of the cell [35].

4.2.2 Photoproduction Background

Even after the trigger selection, there can be some remaining photoproduction events still in the DIS data sample, which are characterized by the absence of a scattered electron in the calorimeter. In order to eliminate them, the SINISTRA [36] neural network based electron finder information was used. Three cuts are made in order to do so. First, the energy deposited by the scattered electron is again required to be greater than 4 GeV ($E_e > 4$ GeV) to re-impose the TLT cut. Secondly, the probability provided by the electron finder of the candidate has to be greater than 0.9. Finally, momentum conservation gives rise to the quantity $E - p_z$ (see section 4.1.2 for details) which allows us to eliminate photoproduction background by requiring $E - p_z > 40$ GeV. These cuts don’t ensure that absolutely no photoproduction events will be in the sample, but it removes a good part of them.

4.3 Cleaning Cuts

To select vector mesons events out of the DIS sample, more specific requirements were placed. In this analysis, we used the decay channel $V \rightarrow \pi^\pm \pi^\mp$. The vector mesons cannot be detected directly, but the decay products are measured by the tracking system. We are then looking for at least two tracks per event for the two pions. Considering that the mesons are resonances, hence very short lived, the tracks have to originate from the primary vertex. It is

also required that no secondary vertex should be found since the pion should be stable inside the CTD volume. Further requirements are explained below.

4.3.1 Vertex Position

A cut is applied on the z -position of the primary vertex. This is done in order to reduce more accurately the background coming from proton beam-gas interaction and cosmic showers. This background is also suppressed by timing cuts at the FLT level. For this analysis, a cut of $|z_{vtx}| < 35$ cm was applied, $z = 0$ being the nominal interaction point (see figure 4.2).

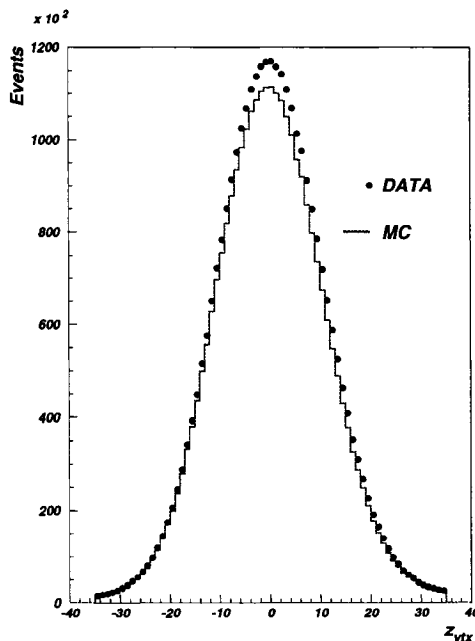


Figure 4.2: *Vertex position comparison between data and reweighted Monte Carlo.*

4.3.2 Transverse Momentum

In addition to the vertex cut, the transverse momentum of the tracks is also used to reduce background. Tracks with higher p_T are also less disturbed by detector effects. With $p_T > 0.15$ GeV for tracks coming from the primary vertex as mentioned above, we make sure to select only good tracks and good pion candidates.

4.3.3 Angular Distribution

Good tracks also have to be located well inside the angular (θ) range of the CTD to have a reasonable number of hits. A common measure in ZEUS is to require that the track had passed through at least 3 superlayers of the CTD. Particularly here, we request the tracks to be located inside $27.5^\circ < \theta < 149^\circ$ or, more precisely using pseudorapidity, $-1.3 < \eta < 1.4$, where pseudorapidity is defined as $\eta = -\ln(\tan(\theta/2))$.

4.3.4 Phase Space

Cuts performed on the variables involving the energy transferred to the partons during the collision are known as *Phase space cuts*. Such variables are the photon virtuality (Q^2) or the fraction of momentum transfer (y). Since these variables cannot be measured directly, they need to be reconstructed using the information we can measure for the event. Different methods exist to do this task. Only the ones that were used will be presented and described.

Deep inelastic scattering events are defined as events with a photon virtuality greater than 1 GeV² ($Q^2 > 1 \text{ GeV}^2$). On the other hand, photoproduction events have $Q^2 < 1 \text{ GeV}^2$. Here is a summary of the phase space cuts for this analysis.

- $Q^2 > 3 \text{ GeV}^2$: Since the simulated events have a higher cut on photon virtuality ($Q^2 > 2 \text{ GeV}^2$), the cut was raised to 3 GeV² to avoid problems at the boundary. This allows a better comparison between data and Monte Carlo as well as preserving a good amount of low Q^2 events. The electron method, which involves the scattered electron information, is used to reconstruct Q^2 . It is more efficient for DIS events, where we have the electron information available [10].

$$Q_e^2 = 2E_e E_e' (1 + \cos\theta_e') \quad (4.1)$$

- $y_{JB} > 0.02$: The Jacquet-Blondel method is a reconstruction method involving the hadronic information from the calorimeter. It uses the

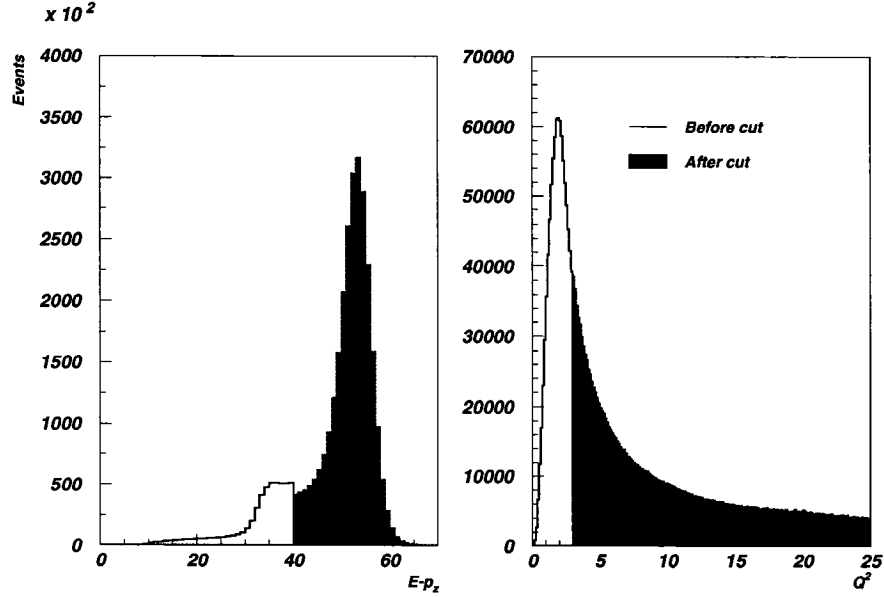


Figure 4.3: Graphical view of two cuts, Q^2 and $E-p_z$ with the number of events before and after the cut was applied. The mismatch in the $E-p_z$ distribution is caused by contamination of events that were not discarded by the other cuts.

following formula to reconstruct y , the fraction of electron energy transferred to the proton in the collision [37]:

$$y_{JB} = \frac{1}{2E_e} \sum_{cells} (E - p_z)_h \quad (4.2)$$

This helps to reject more beam-gas events, which tend to have a low y_{JB} value. Neutral Current DIS events have values around 1.

To calculate y_{JB} , information from the calorimeter was used. Note that this is the only variable in this analysis using such information. Energy from the calorimeter should normally be corrected due to deposit of energy in dead material, using simulated data. Since the y_{JB} cut is negligible in the present analysis ($\mathcal{O}(10^{-3})$), such energy corrections were not necessary.

- $y_e < 0.95$: The electron method describes y as:

$$y_e = 1 - \frac{E'_e}{2E_e}(1 - \cos\theta'_e) \quad (4.3)$$

Rejecting high values of y_e helps to eliminate photoproduction events, for which the electron scatters at a very small angle. The scattered electron energy used in this formula was corrected for dead material.

5 Event Simulation

Simulated events in high energy physics are essential because they play two important roles. First, they allow us to have a better understanding of our detector. As a measurement device, a detector can never be perfect: particles can deposit energy in dead material or be misidentified for example. These are the so-called *detector effects* and they have to be taken into account in our calculations. Since a lot of events will be produced but not detected, we need to scale the cross section measurements with the *acceptance* of the detector, in order to obtain a detector-independent number, as a cross section should be. This can only be estimated using event simulations, the so-called *Monte Carlo* (MC) simulations, since they are probability-based.

Secondly, MC simulations are a way to compare data to a theoretical model. Since the fragmentation (hadronisation) stage, at which partons combine to form hadrons, is not yet well understood in high-energy collisions, the simulations allow to test different suggested models with data and draw conclusions from them.

An event simulation is divided into two important parts: the event generation, where the events are produced and recorded as four-momentum objects, and detector simulation, where the events are passed through a modelled detector to obtain objects that are comparable to data format, i.e. tracks, energy deposit in the calorimeter, etc.

5.1 Event Generation

The event generation is divided into several steps. First is the *hard scattering*, the collision, at which point the two incoming particles are interacting via a leading order Feynman diagram, giving outgoing particles as an output for the next step. The products are partons, i.e. quarks and gluons. They are then input to the *parton shower* step, where they are allowed to split and to radiate gluons. The initial state radiation is also computed at that stage. The shower goes on until the particles reach a predetermined threshold virtuality. All the resulting partons are then forming colorless hadrons at the *hadronisation* or

fragmentation stage. This is a non-perturbative process of QCD and it is still not well understood in terms of theory. It is then calculated using different phenomenological models. [38]

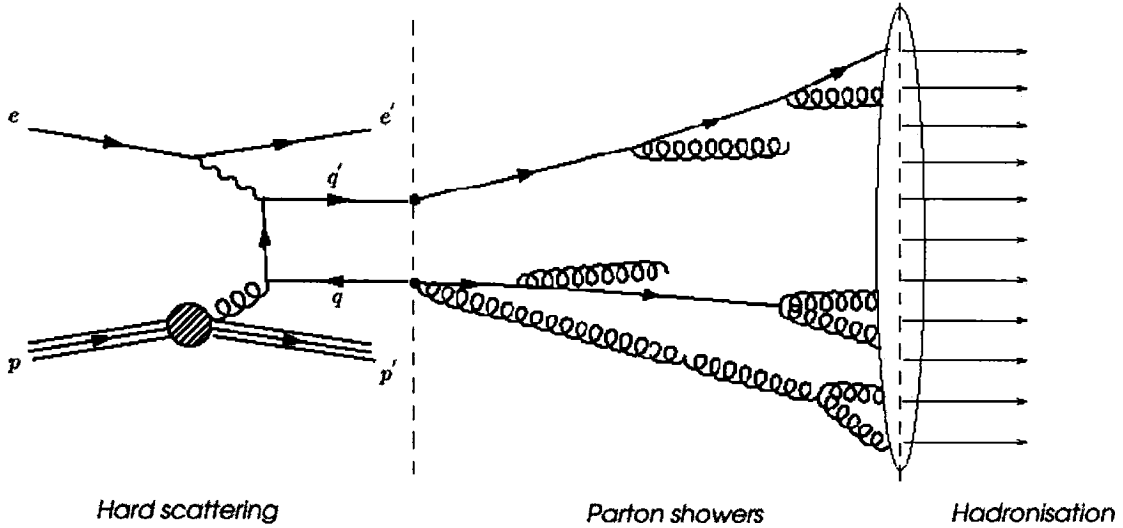


Figure 5.1: Event generation diagram where the three phases are shown in the case of a boson-gluon fusion (BGF) event. From left to right: hard scattering, parton shower and hadronisation

5.2 ARIADNE-flavoured DJANGO

The MC generator used for this analysis is DJANGO 1.1. DJANGO is a combination of DJANGO[39] and HERACLES. It is an interface to deep inelastic event generator for lepton-proton interactions, developed in DESY. It uses HERACLES 4.6.1 [40], a neutral and charged current DIS events generator. HERACLES also includes radiative and one-loop corrections and it is interfaced to LEPTO 6.5.1 [41] for fragmentation. The proton PDF (parton distribution function) used in this sample is CTEQ5L [42] for leading order, used to simulate the structure functions.

The parton shower is computed by the program ARIADNE 4.10 [43]. It uses the Colour Dipole model [44]. This model states that the gluon radiating from a $q\bar{q}$ pair can be treated like the radiation from a color dipole. The radiated gluon can then be combined with one of the two original quarks to form

another dipole, which can radiate another soft gluon. This new gluon will then give rise to a third color dipole, and so on. In this model, the ordering in time of the cascade is done using p_{\perp}^2 (the parton transverse momentum), which means that the first branching products have the greatest p_{\perp}^2 and the last branching, the smallest p_{\perp}^2 . This parton shower is also interfaced to LEPTO, to allow the fragmentation to be computed.

LEPTO makes use of the Lund string fragmentation scheme [45]. In this model, the two outgoing quarks are going away from each other, but are linked by a color field. The strength of this field increases with distance. Unlike the electromagnetic field, the color field is constrained to a tube-like shape, which forms the *string*. When the energy contained in the string is large enough, the string breaks, forming two new quarks. This fragmentation continues until there is not enough energy in the string to form new particles, hence leaving the remaining colorless hadrons. These final state hadrons are then ready for the detector simulation.

Only one sample was used (compared to two normally) due to time constraints. A second sample from HERWIG could have been used in order to verify results obtained for ARIADNE. The analysis does not suffer from it since such an inclusive sample is generally well understood.

5.3 Detector Simulation

To properly simulate the ZEUS detector, a program that models the materials and the volumes is needed as well as a facility to obtain data-like format to be able to use it with the same code as data, allowing a proper comparison between the two samples. This combination for ZEUS is called MOZART.

The MOZART simulation is a GEANT-based model [46] of the ZEUS detector. GEANT simulates the passage of particles through matter by assigning a medium to a specific volume, with all the associated properties of that medium. It is thus not limited to applications in high energy physics. It simulates electromagnetic and hadronic showers, the magnetic field, the tracks and

the hits in all detectors and records them.

The MOZART (MOnte Carlo for Zeus Analysis, Reconstruction and Trigger) interface outputs data-like quantities which are then sent to the ZEUS trigger simulation, ZGANA. This will associate trigger bits to the simulated events, so that the bits can be requested in the analysis code. The output of ZGANA, like the real data, is sent for complete reconstruction to ZEPHYR (ZEus PHYsics Reconstruction). A large amount of computers all over the world, from different institutes from the collaboration, are dedicated to compute these events. This is called *Funnel*, the ZEUS MC production facility.

5.4 DIS Sample

For this analysis, a fully inclusive neutral current DIS sample of 23 million events was used. The 2000 MOZART version was used, which is representative of the running period 1998-2000 because no major changes were done to the hardware in that period. It has a luminosity of 55.04 pb^{-1} and contains events with $Q^2 > 2 \text{ GeV}^2$ and $y > 0.01$. It uses a positron as the incoming lepton.

6 Meson Production Analysis

The aim of the present analysis is to extract the cross section for three meson resonances, ρ^0 , $f_0(980)$ and $f_2(1270)$. The different steps of the analysis are presented below. The first thing to verify is that the chosen Monte Carlo sample describes the data for standard kinematical quantities. Once this is confirmed, one can proceed in extracting the signals for the resonances and calculate the detector corrections that will later on be applied to the cross sections. The differential cross-sections are then calculated as a function of η and p_T .

6.1 Monte Carlo vs Data

As described in section 5, a simulated fully inclusive neutral current DIS sample of low Q^2 events was used to compare with the data.

6.1.1 Control Plots

Control plots are histograms that compare data and simulated events for known variable distributions at the detector level. The goal of this procedure is to verify the agreement of the simulation with data. If this is verified, it is then allowed to use the simulated data to extrapolate information on the data back to the hadron level, i.e. at a level where we can't directly measure. A choice of kinematic and tracking variables was made for this analysis. Tracking variables, such as multiplicity of tracks or angle of tracks, are important since we work mainly with tracks to identify the pions. Also, basic kinematic variables are verified to get a broader view of the agreement.

As can be seen from figure 6.1, there seems to be large disagreements between data and Monte Carlo. This disagreement comes from the prescale effect, as mentioned in section 4.1. The trigger selection used for the data involves a prescaling, while the simulated trigger does not need this purely online feature. This induces a discrepancy in the event selection between the real and simulated data that can be partially recovered, as explained in the next section.

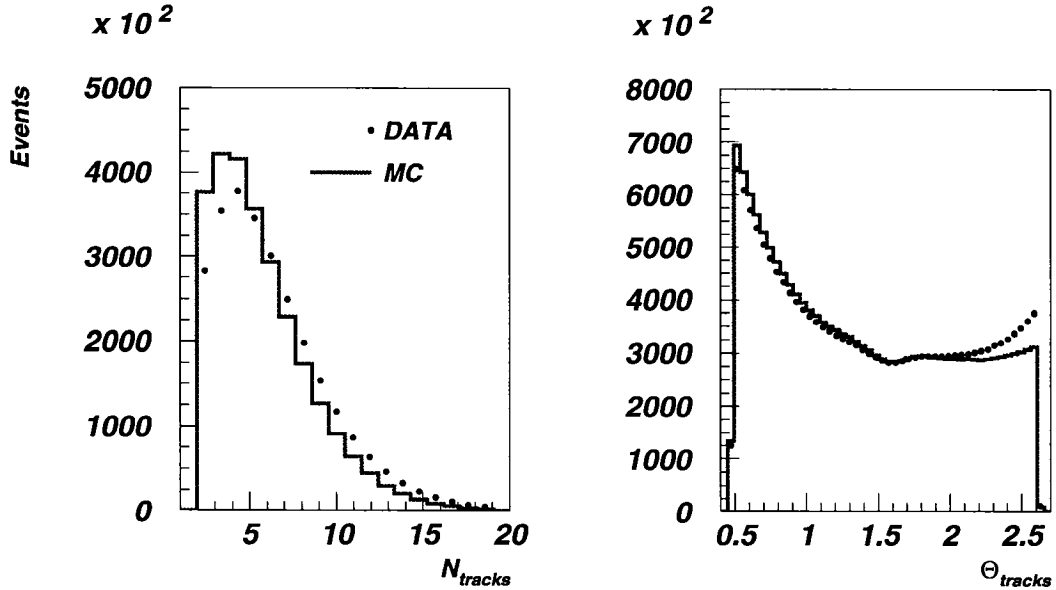


Figure 6.1: Control plots before reweighting. Monte Carlo is normalized to data.

6.1.2 Monte Carlo Reweighting

The disagreement seen in the control plots of section 6.1.1 can be explained by the prescaling effect. During data taking, it happens that the amount of good physics data to be dealt with by the trigger is too big and causes *deadtime* (time during which the trigger is busy making computations and no data can be acquired). The deadtime is something one always want to keep as low as possible. A solution is then to put only a fraction of this data on tape, so that only one event in n are taken, where n is then the prescale factor. For the running period of interest, the prescaling was done on both DIS01 and DIS03 triggers, at low Q^2 , in two different ways. For DIS01, the prescale factor n was changed from run to run. For DIS03, the radius cut, hence the Q^2 threshold, was changed, in order to take less low Q^2 events. The latter is not a prescale by definition, but the effect of that change is the same, i.e. less events are taken.

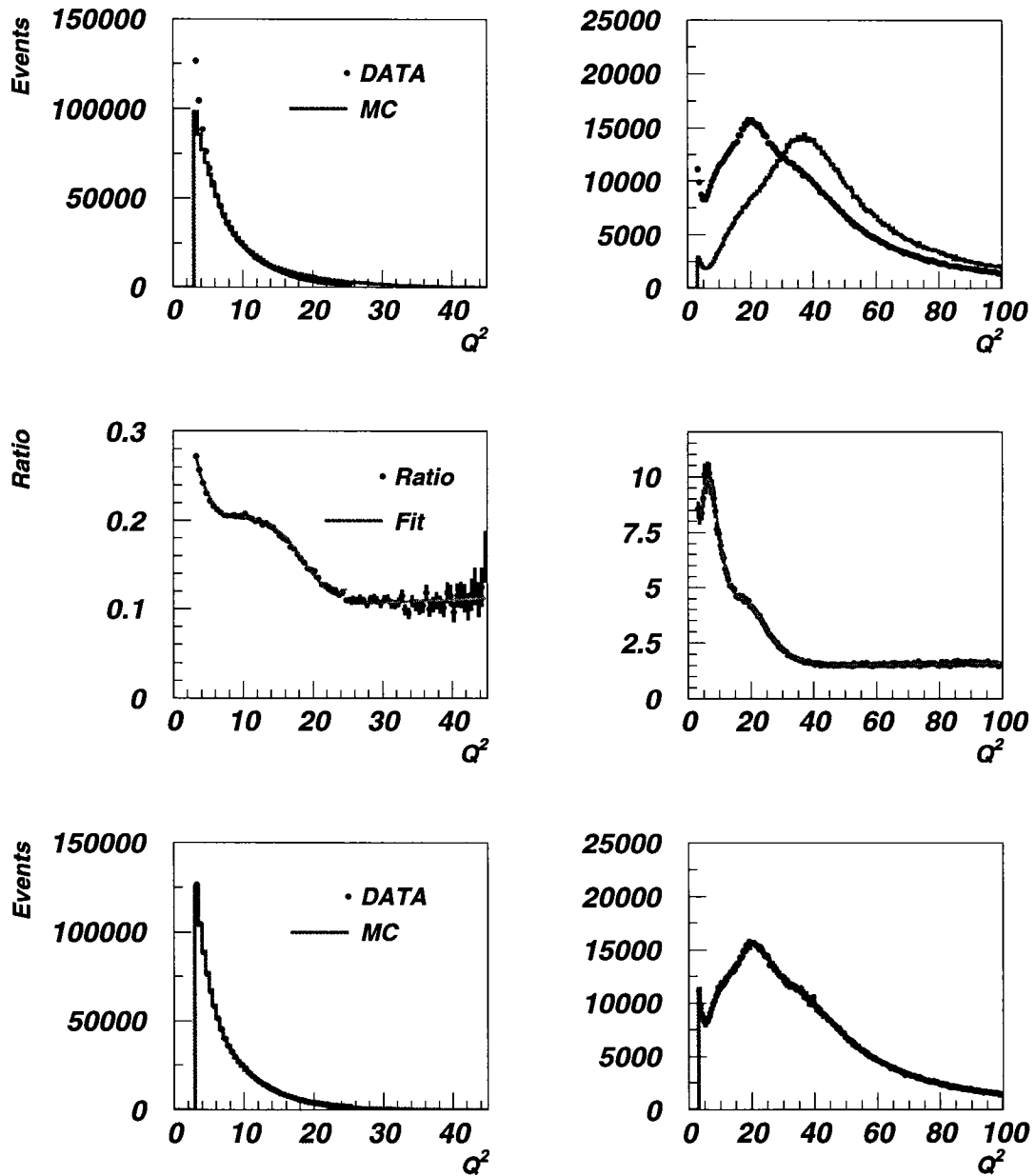


Figure 6.2: *The top plots show the Q^2 distributions before reweighting, the middle plots are the weight factor fits and the bottom plots are the Q^2 distributions with only the Monte Carlo events reweighted to match the data. The left-hand side is for the DIS01 trigger case and the right-hand side is for DIS03 trigger.*

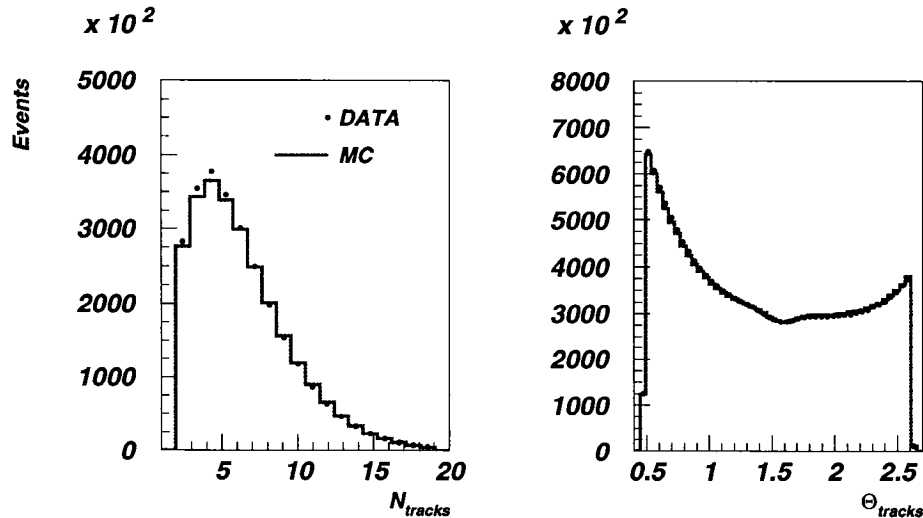


Figure 6.3: *Reweighted control plots using previous fit. The agreement between data and Monte Carlo is better after the reweighting compared to figure 6.1.*

In order to take care of these two different effects, DIS01 and DIS03 events were considered separately. In each case, the weights were evaluated using the Q^2 distribution for data and Monte Carlo. The ratio between data and Monte Carlo values was plotted and fitted as shown in figure 6.2. The fit was done in two separate sets of bins, using a polynomial part and a flat line. The boundary is different for each trigger, being $Q^2 = 25 \text{ GeV}^2$ for DIS01 and $Q^2 = 40 \text{ GeV}^2$ for DIS03. It can be seen that there is a slight discontinuity at the boundary (larger in the case of DIS01) but this does not create problems, since it covers only a very small portion of the data and the weight factors are allowed to vary within a reasonable interval. From the fit, weight factors were extracted and applied to the Monte Carlo distribution as shown on the bottom plots of figure 6.2. Since Monte Carlo is simulated data, an arbitrary weight can be applied to the events without changing the physics meaning behind it, which is not the case with the data. The weight factors were then applied to the tracking variables, as can be seen in figure 6.3. The agreement is improved and the simulated data can then be used for further analysis.

6.2 Signal Extraction

The three resonances are studied in their $\pi^+\pi^-$ decay channel, which is the dominant one for all of them. The goal is then to find two tracks among all the tracks in the selected events that will be good pion candidates. First, the reflection signals are extracted and then the invariant mass spectrum for the 2-track combinations is obtained. The reflections are then subtracted before the fit of the resulting spectrum.

6.2.1 Reflections

Reflections are decays that might interfere with the desired ones due to imperfections of the detector. Basically, anything that can decay to two oppositely charged pion candidates in the targeted mass range can be a potential reflection. Of course, depending on the mass, branching ratio and cross section of the decay, only a few are really important to be considered.

In the present case, two reflections were considered to be important.

- $K^*(892) \longrightarrow K^\pm\pi^\mp$
- $\omega(782) \longrightarrow \pi^\pm\pi^\mp\pi^0$

For the K^* meson, the final state kaon may have been misidentified as a pion, and causing it to be chosen in the track selection and included in the $\pi\pi$ spectrum. For the ω meson, the π^0 may not have been detected by the calorimeter, hence mistaking this meson for a ρ^0 in the spectrum. Both these mesons have a mass close to the ρ^0 mass (770), so their contribution will be mainly affecting the first peak. The possible reflections that would affect f_0 (980) and f_2 (1270), for example $\phi(1020)$ and $\eta'(958)$, have very small production rates and can therefore be neglected.

The shapes of the reflections were obtained from the Monte Carlo events since the hadron level information is needed to study detector effects. The K^* and ω mesons that decayed into two pions of any charge were selected. After this selection, a matching in the η - ϕ space of the detector tracks with

the four-momentum vectors of these pions was performed. A track and a pion were matched if the following condition was satisfied:

$$\Delta_{\eta\phi} = \sqrt{(\eta_{track} - \eta_{MC})^2 + (\phi_{track} - \phi_{MC})^2} \leq 1 \quad (6.1)$$

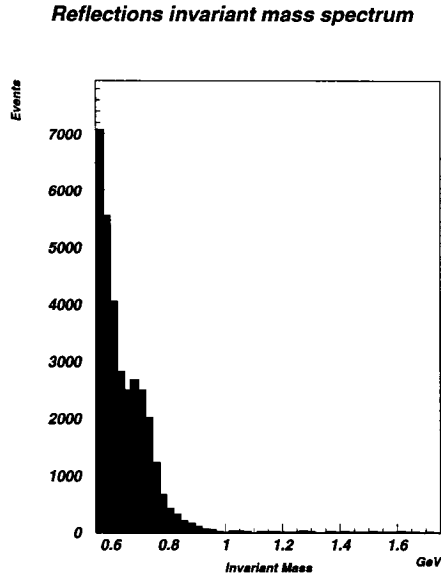


Figure 6.4: *Invariant mass spectrum of the normalized reflection signals. The left peak corresponds to the ω reflection and the smallest peak can be attributed to K^* .*

$\Delta_{\eta\phi}$ was also requested to be minimized, which means that, for each simulated particle, the quantity $\Delta_{\eta\phi}$ was calculated with every track in the event and only the track with the smallest $\Delta_{\eta\phi}$ value was considered. The requirement of equation 6.1 is only applied to this minimized value. The invariant mass was then calculated for the single pair of tracks in the event for which these conditions were fulfilled. The spectrum is shown in figure 6.4. The details of the invariant mass calculation are given in the next section.

The reflections taken from the Monte Carlo were normalized to the ρ^0 peak. The total number of pairs of tracks contained in the reflection spectrum was compared to the fitted number of ρ^0 in the Monte Carlo 2-track invariant mass spectrum. The ratio was measured to be 0.07 ± 0.02 .

6.2.2 Invariant Mass Spectrum

In order to find if a resonance was produced, the energy-momentum of the decay product tracks is used to calculate their invariant mass. The invariant mass can be derived from relativistic energy-momentum equation; it is independent of the frame of reference and can therefore be used without a boost in the center of mass frame. It has the following form:

$$I_{mass} = \sqrt{\left(\sum_i E_i\right)^2 - \left(\sum_i \vec{p}_i\right)^2} \quad (6.2)$$

All 2-track combinations were used to calculate their invariant mass and only those for which the mass was in the range 0.55 GeV - 1.75 GeV were considered, to avoid contamination of the spectrum by kaons, for which the mass is smaller than 0.55 GeV. In the calculations, the pion mass (139.57018 ± 0.00018 MeV) was assumed. If the track was not a pion, then the invariant mass would be outside the allowed range for the three resonances. The specific form of the invariant mass for the two-pion case is shown here.

$$I_{mass} = \sqrt{2 \times \left(m_\pi^2 + \sqrt{m_\pi^4 + m_\pi^2(p_1^2 + p_2^2)} + p_1^2 p_2^2 - \vec{p}_1 \cdot \vec{p}_2\right)} \quad (6.3)$$

In the latter, \vec{p}_1 and \vec{p}_2 are the momentum vectors of each track in the pair and m_π is the rest mass of the charged pion.

A first background subtraction was done by making two different invariant mass distributions: one with two tracks of the same charge ($\pi^-\pi^-$ or $\pi^+\pi^+$) and one with the tracks of different charges. The same-charge plot forms the *combinatorial background* and should be subtracted from the different-charge plot. Once this is done, the peaks can be seen above the residual background.

The resulting invariant mass spectrum can then be fitted using a three-part fit function.

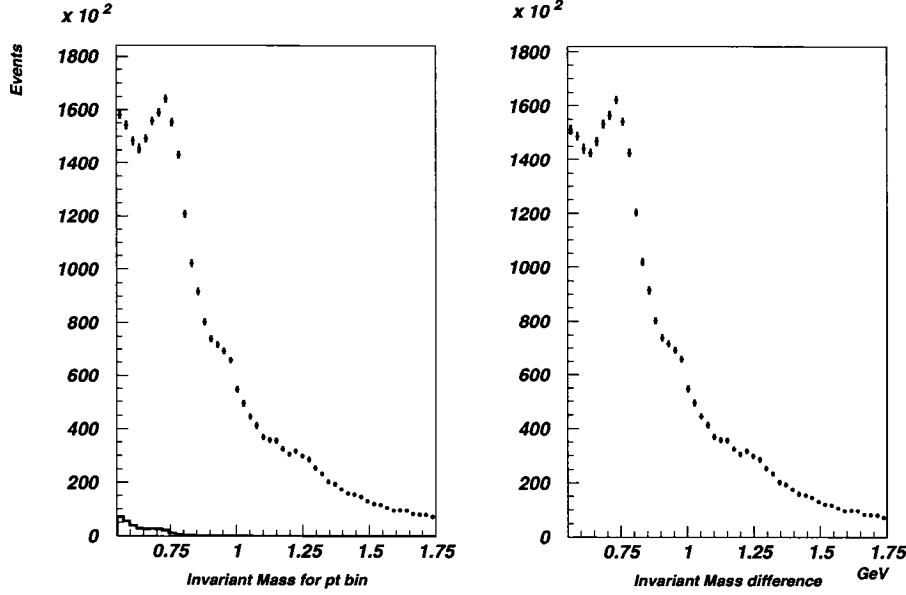


Figure 6.5: *2-track invariant mass spectra. The left plots shows the distribution before reflections subtraction (with the reflections shown) and the right plot, after reflections subtraction.*

$$Fit(m) = bkg(m) + \sum BW(m) + \sum ref(m) \quad (6.4)$$

Equation 6.4 corresponds to the residual background, the resonance signals and the reflections, respectively. Since the reflections are obtained directly from the Monte Carlo events, no fit was necessary. The reflections spectrum (figure 6.4) was subtracted from the 2-track spectrum. The resulting distribution, on which the fit was performed, is shown in figure 6.5. The statistical error propagation was done at each spectrum subtraction. The errors of each subtracted spectrum were added in quadrature to give the resulting errors.

The background fit function is an exponential function of the form:

$$Bkg(m) = p_1(m - 2m_\pi)^{p_2} e^{-p_3 m - p_4 m^2} \quad (6.5)$$

where m_π is the charged pion rest mass and p_i are free parameters. The three peaks are fitted using a relativistic Breit-Wigner function [47].

$$BW(m) = C \frac{m_0 m \Gamma(m)}{(m^2 - m_0^2)^2 + m_0^2 \Gamma^2(m)} \quad (6.6)$$

where

$$\Gamma(m) = \Gamma_0 \left(\frac{q}{q_0} \right)^{2l+1} \frac{m_0}{m} \quad (6.7)$$

In the latter, l is the angular momentum of the particle, which is $l = 0$ for f_0 , $l = 1$ for ρ^0 and $l = 2$ for f_2 . Γ_0 is the nominal particle width. All the masses and widths were taken as free parameters in the fit, except for the f_0 width which was fixed at 100 MeV, from the Particle Data Group [16]. This width is allowed to vary within a broad interval in the systematic errors calculation (see section 6.4.4). The variable q stands for the momentum of the decay products (here, the pions) in the rest frame of their parents, the mesons. Since q is really $q(m)$, q_0 would then be $q(m_0)$, the function evaluated at the nominal resonance mass. As calculated from simple kinematics, $q(m)$ has the form:

$$q(m) = \sqrt{\frac{m^2}{4} - m_\pi^2} \quad (6.8)$$

Figure 6.6 shows the total fit before and after the final background subtraction. In order to extract the number of particles from the fit, the following parametrization has been applied to the fit parameters C of the Breit-Wigner shapes.

$$C = N \times \Delta m \quad (6.9)$$

where N is the number of events for each resonance and Δm is the bin size for the invariant mass. Here the bin width was set to 24.4 MeV, which corresponds to the same number of bins as H1 [17]. This procedure can be applied since the integral of a probability distribution from $-\infty$ to ∞ is equal to one. The results obtained from the fit of the invariant mass spectrum are shown in table 6.1.

2-track invariant mass spectrum

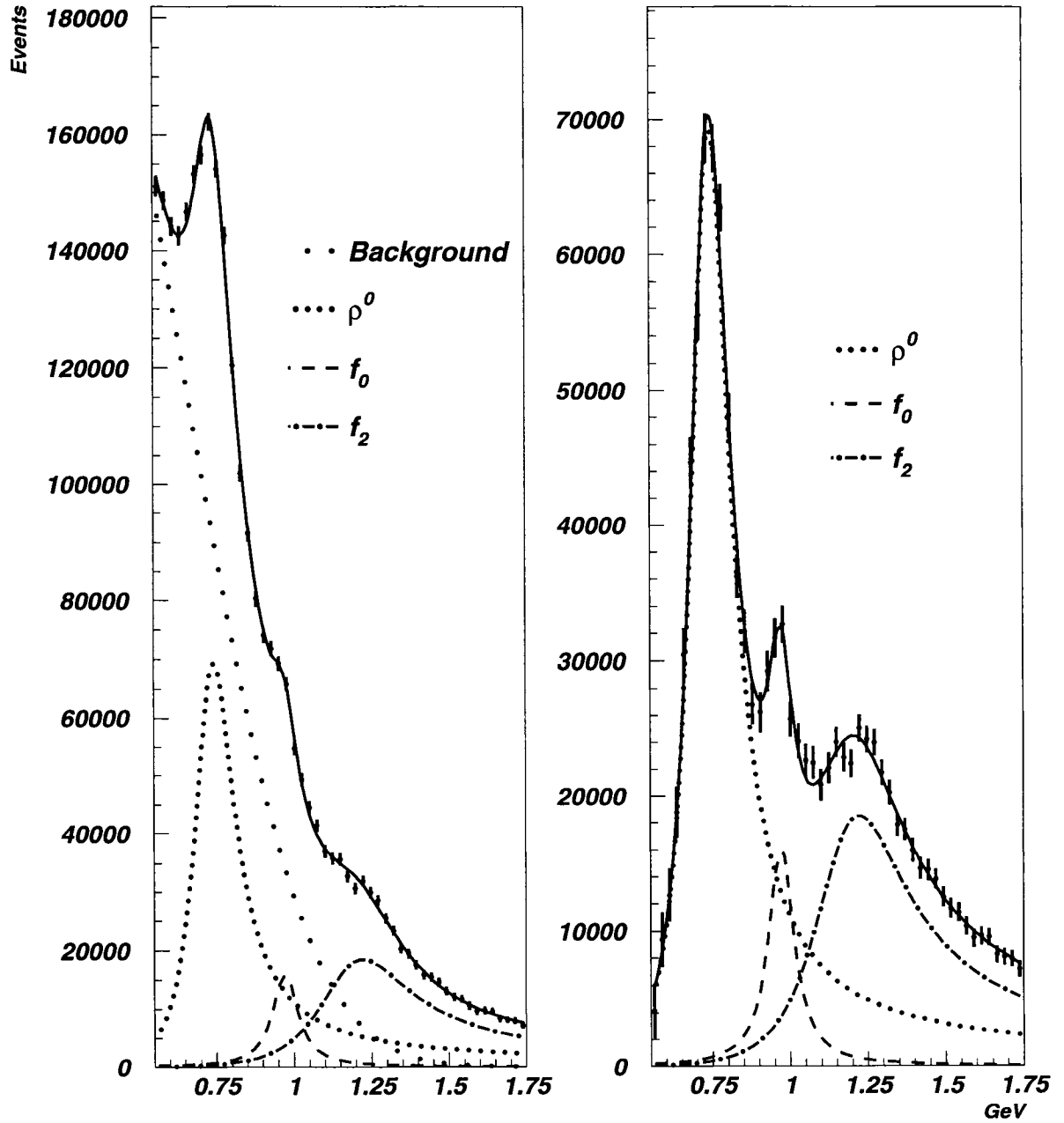


Figure 6.6: Fit of the invariant mass spectrum. The left plot shows the total fit (solid line) with the curves for each signal and the combinatorial background (dotted line) explicitly shown. The right plot is the refit (solid line) of the left plot with the combinatorial background subtracted.

Parameter	ρ^0	f_0	f_2
Mass (GeV)	0.750 ± 0.001	0.970 ± 0.003	1.283 ± 0.012
Mass from PDG (GeV)	0.771 ± 0.001	0.970 ± 0.010	1.275 ± 0.001
Γ (GeV)	0.165 ± 0.008	0.100	0.600 ± 0.053
Γ from PDG(GeV)	0.149 ± 0.001	0.040 to 0.100	0.185 ± 0.003
N	466687 ± 35739	65323 ± 6016	409008 ± 26038

Table 6.1: *Parameters obtained from the fit of the invariant mass spectrum for the three mesons. N is the number of events. The f_0 width was fixed to 100 MeV. The errors shown on the fit parameters are only statistical.*

It can be noticed, looking at the results for the mass value in table 6.1, that the ρ^0 peak is slightly shifted to the lower masses. It has a value closer to 750 MeV instead of the 770 MeV, which is the accepted value from the Particle Data Group [16]. This can be explained using Bose-Einstein correlations and energy threshold cuts (0.55 GeV) that would affect the position of the peak when fitted. They manifest themselves by an enhanced production of pion pairs with similar momenta. This effect has been studied in previous measurements of neutral meson production at LEP [48]. On the other hand, the f resonances accepted mass values are within the errors.

6.3 Detector Corrections

Corrections have to be applied to the data in order to deal with imperfections of the detector. These imperfections can come from several sources. The detector itself can be missing some signals due to electronics problems or the precise reaction could simply not be detected with this type of detector (due for example to short lifetimes, dead material or inefficiencies). The net effect is that more particles are produced at the hadron level than what is seen by the detector and the results cannot be compared to the theoretical predictions unless the acceptance of the detector is determined.

In order to compute the acceptances, we need to be able to compare directly theory and experiment; that is where Monte Carlo simulations come to help. For the present analysis, only one of the three mesons was produced in

Monte Carlo models, the ρ_0 . For the other resonances, the reconstruction of all $\pi^+\pi^-$ pairs was used as an estimate of their acceptance. The computed acceptances for the three mesons are presented in table 6.2. Details of their computation can be found below.

	ρ^0	f_0	f_2
Acceptance	$29.4 \pm 0.4 \%$	$125 \pm 2 \%$	$161 \pm 3 \%$

Table 6.2: *Acceptances for the three mesons.*

The absolute number of particles at the hadron level was obtained from the Monte Carlo and was compared to the measured number of particles. In the case of the ρ^0 , the latter was obtained from the fit of the Monte Carlo reconstructed tracks invariant mass spectrum. The fit of the Monte Carlo spectrum was done according to the procedure presented in section 6.2.2. The acceptance was calculated using the following equation.

$$A = \frac{\epsilon}{p} = \frac{N_{meas}}{N_{gen}} \quad (6.10)$$

where N_{meas} is the number of measured events and N_{gen} is the number of generated events. The efficiency ϵ and the purity p are also used to characterize the data sample and are defined below.

$$\epsilon = \frac{N_{meas} \cap N_{gen}}{N_{gen}} \quad (6.11)$$

$$p = \frac{N_{meas} \cap N_{gen}}{N_{meas}} \quad (6.12)$$

In the case of the ρ_0 , the peak was fitted to obtain the number of measured events. Since f_0 and f_2 are not generated by the Monte Carlo simulation, the acceptance for $\pi^+\pi^-$ pairs was considered instead. The number of generated and reconstructed $\pi^+\pi^-$ pairs were obtained from the Monte Carlo to evaluate the efficiency of $\pi^+\pi^-$ pairs. Using the equation below, the correction factor was calculated for the f resonances. The correction factor is defined as the inverse of the acceptance and ϵ is the efficiency. The superscript i is either f_0 or f_2 . The efficiency of the pion pairs was calculated in the mass region

corresponding to each meson. For f_0 , a mass window of $0.8 < I_{mass} < 1.1$ was considered and for f_2 , $1.1 < I_{mass} < 1.5$.

$$C \equiv \frac{1}{A} = \frac{\epsilon^i}{\epsilon^{\rho^0}} \quad (6.13)$$

In evaluating the correction factor in this fashion, the values for the acceptance shown in table 6.2 are very high (i.e. completely unphysical) for the two non-simulated mesons (see section 6.4). Since the acceptance is higher than its real value should be, the cross section will get underestimated. This way, the results for the cross sections, instead of being accurate, are a good minimal evaluation of what should be measured with a proper simulation.

6.4 Cross Section Measurement

Once the number of events and the acceptance for each meson are measured, the next step is to measure the cross sections. The cross section is a measure of the probability for a certain process to happen. It serves as a link between experimental data and theoretical models to confirm or disprove the latter. In the following sections, the results for the ρ^0 , f_0 and f_2 mesons are presented.

6.4.1 Total Cross Sections

The measured cross section has the following form:

$$\sigma = \frac{N}{A \times \mathcal{L} \times Br} \quad (6.14)$$

N is the number of events measured, A is the acceptance in the detector, \mathcal{L} is the total luminosity for the running period 1998-2000 and Br is the branching ratio for the chosen decay channel from the Particle Data Group [16].

In order to calculate the cross sections, the parameters obtained from the previous fit, shown in table 6.1, are used. The common decay channel used for this analysis, $\pi^+\pi^-$ is evaluated to have a branching ratio of 100 % in the ρ^0 case. For the f_0 meson, the decay mode is said to be dominant, so its branching ratio is approximated to 100 %. Finally, the f_2 meson has a branching ratio of $0.848^{+0.025}_{-0.013}$. The total luminosity for the 1998-2000 running period was

measured to be $82555 \pm 1054 \text{ nb}^{-1}$. The results for the total cross section calculations for each mesons are shown below. The details for the calculations of the systematic errors are discussed in section 6.4.4.

$$\begin{aligned}
 \sigma_{\rho^0} &= 19.21 \pm 0.92 \text{ (stat.)} \pm 7.59 \text{ (syst.) nb} \\
 \sigma_{f_0} &= 0.63 \pm 0.04 \text{ (stat.)} \pm 0.25 \text{ (syst.) nb} \\
 \sigma_{f_2} &= 3.62 \pm 0.02 \text{ (stat.)} \pm 1.73 \text{ (syst.) nb}
 \end{aligned}
 \tag{6.15}$$

As explained in section 6.3, the σ_{f_0} and σ_{f_2} values and their corresponding differential cross sections (see below) must be considered as underestimates.

In order to study the behaviour of the cross sections as a function of two variables, the transverse momentum p_T and the pseudorapidity η , differential cross sections have been extracted and are presented in sections 6.4.2 and 6.4.3. The following binning was used.

- p_T : Six unequal bins ranging from 0 GeV to 7 GeV, as follows, $0 < p_T < 0.55$, $0.55 < p_T < 0.75$, $0.75 < p_T < 1$, $1 < p_T < 1.5$, $1.5 < p_T < 2$, $2 < p_T < 7.00$. The bins were chosen to get comparable statistics in each bin.
- η : Four equal bins between $\eta = -1$ and $\eta = 1$, to get a geometric view of the cross sections.

6.4.2 Differential p_T Cross Sections

The same fitting procedure was applied to every p_T bin defined previously. The reflections were also extracted bin per bin to be subtracted from the invariant mass spectrum. The resulting mass distributions are shown in figure 6.7. An important difference in the relative importance of the background is to be seen in these plots. At low p_T , it is relatively significant while at higher p_T , its contribution compared to the ρ^0 decreases considerably.

The differential p_T cross sections are shown in figure 6.8. The values for ρ^0 and the f resonances are different by almost an order of magnitude everywhere. It can be seen from this plot that the differential p_T cross section decreases.

p_T range (GeV)	$d\sigma/dp_T[\rho^0]$ (nb/GeV)
0 - 0.55	7.74 ± 0.50 (stat.) $^{+3.63}_{-3.25}$ (syst.)
0.55 - 0.75	4.30 ± 0.30 (stat.) $^{+4.04}_{-3.84}$ (syst.)
0.75 - 1	2.37 ± 0.14 (stat.) $^{+0.73}_{-0.41}$ (syst.)
1 - 1.5	1.79 ± 0.30 (stat.) $^{+0.96}_{-0.95}$ (syst.)
1.5 - 2	0.52 ± 0.10 (stat.) ± 0.22 (syst.)
2 - 7	1.26 ± 0.19 (stat.) $^{+0.35}_{-0.80}$ (syst.)
p_T range (GeV)	$d\sigma/dp_T[f_0]$ (nb/GeV)
0 - 0.55	0.26 ± 0.05 (stat.) ± 0.11 (syst.)
0.55 - 0.75	0.219 ± 0.050 (stat.) ± 0.14 (syst.)
0.75 - 1	0.269 ± 0.023 (stat.) ± 0.14 (syst.)
1 - 1.5	0.270 ± 0.036 (stat.) ± 0.11 (syst.)
1.5 - 2	0.082 ± 0.022 (stat.) ± 0.08 (syst.)
2 - 7	0.138 ± 0.020 (stat.) $^{+0.06}_{-0.04}$ (syst.)
p_T range (GeV)	$d\sigma/dp_T[f_2]$ (nb/GeV)
0 - 0.55	0.804 ± 0.035 (stat.) $^{+0.61}_{-0.56}$ (syst.)
0.55 - 0.75	0.373 ± 0.087 (stat.) $^{+1.10}_{-0.98}$ (syst.)
0.75 - 1	1.196 ± 0.050 (stat.) $^{+0.85}_{-0.81}$ (syst.)
1 - 1.5	2.267 ± 0.099 (stat.) ± 1.45 (syst.)
1.5 - 2	1.474 ± 0.067 (stat.) $^{+0.89}_{-0.87}$ (syst.)
2 - 7	3.11 ± 0.43 (stat.) $^{+1.71}_{-1.40}$ (syst.)

Table 6.3: *Differential cross sections for p_T (actually underestimates for f_0 and f_2 , see section 6.3).*

In the case of f_2 , it is not so clear, since the distribution varies a lot from bin to bin, but within its errors, this statement can still hold. The values for the differential cross sections are presented in table 6.3.

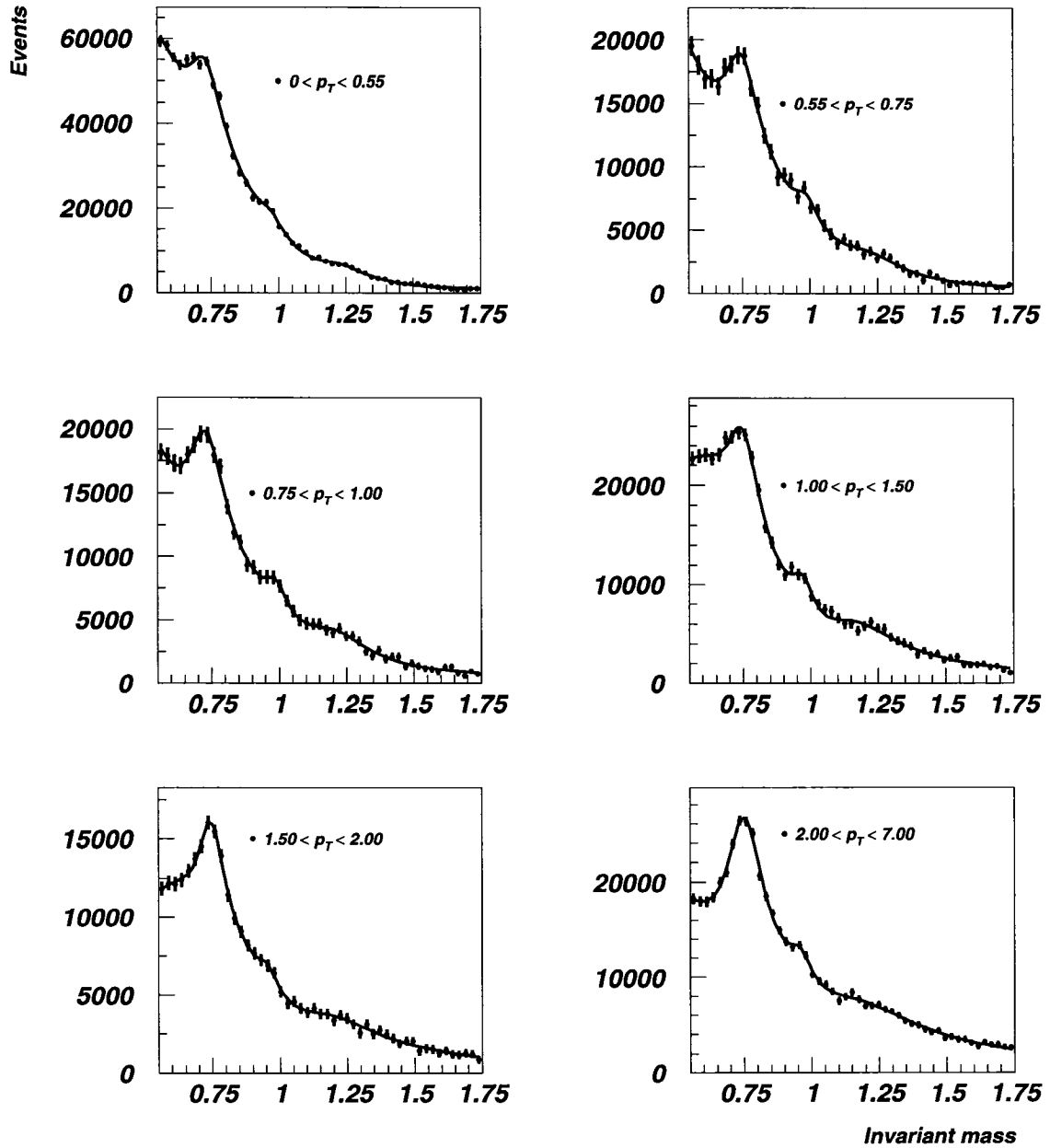
ZEUS 1998-2000

Figure 6.7: *Fit of the invariant mass spectrum in every p_T bin. The reflections have been subtracted in every bin separately. The evolution of the ρ^0 peak compared to the background can be clearly seen.*

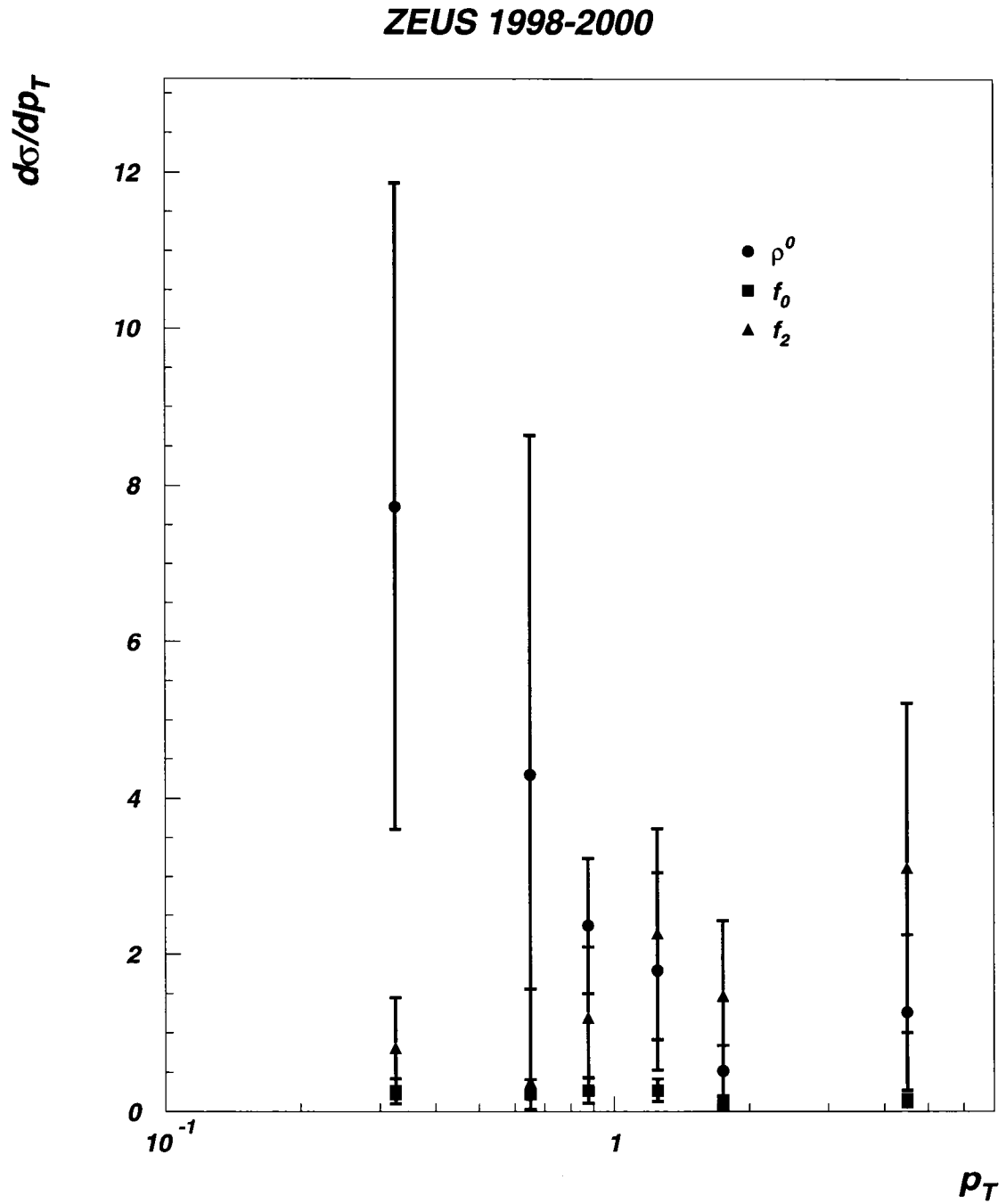


Figure 6.8: *Differential p_T cross sections for the three mesons. The top plot shows the ρ_0 distribution while the bottom plot shows the f_0 and f_2 distributions. The error bars are the sum of the statistical and systematic errors.*

6.4.3 Differential η Cross Sections

The same fitting procedure was applied again in each η bin, as described in section 6.4.1. The results are shown in figure 6.9 and the precise values in table 6.4. Again here, the values for ρ^0 and for the f resonances are considerably different.

η range	$d\sigma/d\eta[\rho^0]$ (nb)	
-1 - -0.5	0.53 ± 0.12 (stat.)	$^{+0.16}_{-0.13}$ (syst.)
-0.5 - 0	0.51 ± 0.09 (stat.)	$^{+0.18}_{-0.17}$ (syst.)
0 - 0.5	0.86 ± 0.08 (stat.)	$^{+0.35}_{-0.23}$ (syst.)
0.5 - 1	0.76 ± 0.11 (stat.)	0.20 (syst.)
η range	$d\sigma/d\eta[f_0]$ (nb)	
-1 - -0.5	0.072 ± 0.011 (stat.)	± 0.12 (syst.)
-0.5 - 0	0.126 ± 0.050 (stat.)	$^{+0.11}_{-0.10}$ (syst.)
0 - 0.5	0.100 ± 0.015 (stat.)	$^{+0.03}_{-0.02}$ (syst.)
0.5 - 1	0.128 ± 0.024 (stat.)	± 0.06 (syst.)
η range	$d\sigma/d\eta[f_2]$ (nb)	
-1 - -0.5	0.58 ± 0.07 (stat.)	$^{+0.47}_{-0.46}$ (syst.)
-0.5 - 0	0.54 ± 0.05 (stat.)	$^{+0.41}_{-0.24}$ (syst.)
0 - 0.5	0.60 ± 0.07 (stat.)	$^{+0.41}_{-0.28}$ (syst.)
0.5 - 1	0.95 ± 0.06 (stat.)	$^{+0.54}_{-0.55}$ (syst.)

Table 6.4: *Differential cross sections for η (actually underestimates for f_0 and f_2 , see section 6.3).*

6.4.4 Systematic Uncertainties

Systematic uncertainties are obtained by letting the cuts on energy and kinematics and fit parameters vary to see the effects on the final results. The distribution is then fitted using the procedure described in 6.2.2. The difference between the cross section value from this new fit and the original one is the systematic uncertainty. The total systematic uncertainties are obtained by doing a quadratic sum of all the sources, thereby assuming that they are uncorrelated. To do so, the following error sources were considered.

- The track transverse momentum cut was varied from $p_T^{track} = 0.15$ GeV to $p_T^{track} = 0.20$ GeV, which is a standard ZEUS value.

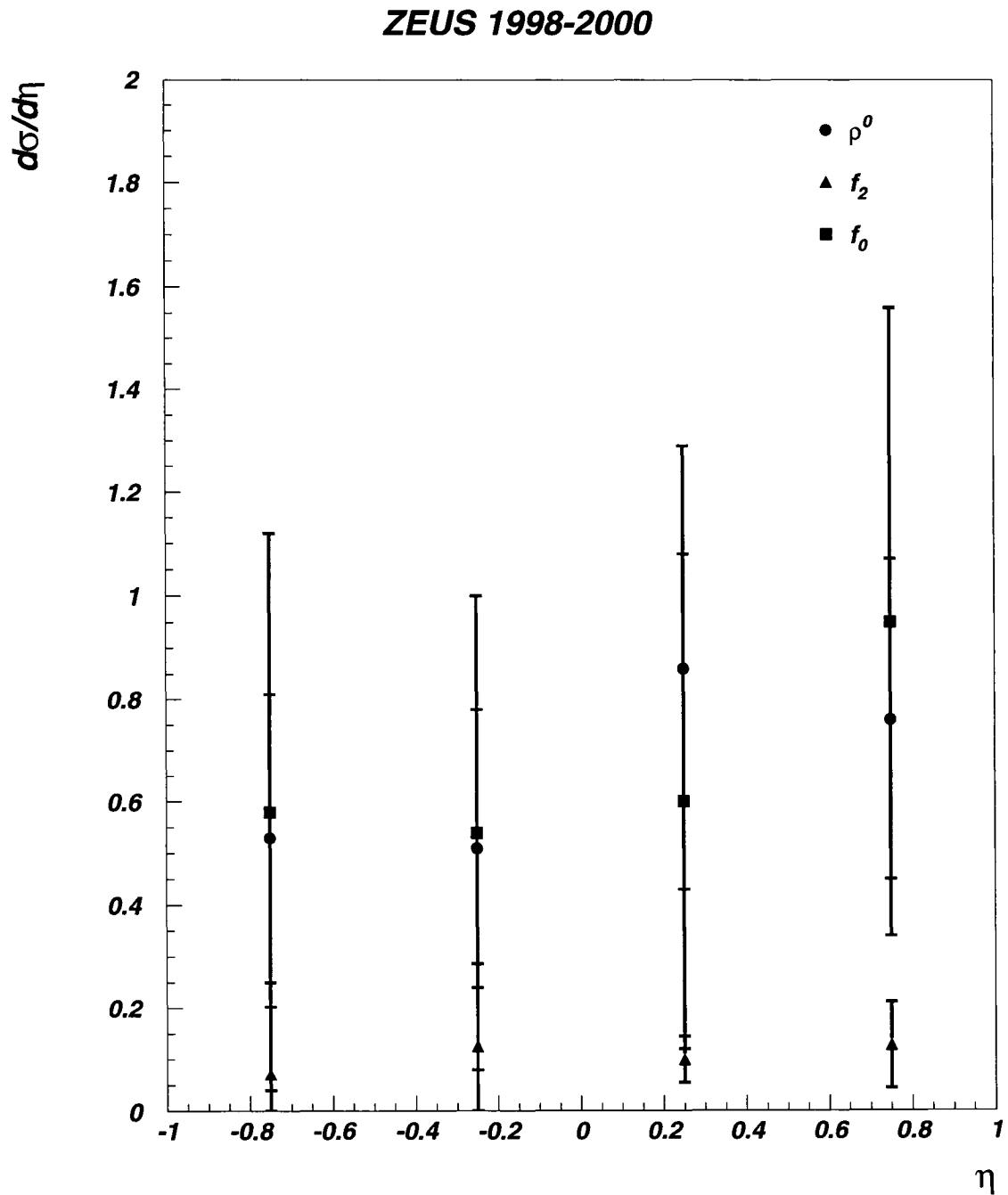


Figure 6.9: *Differential η cross sections. The top plot shows the ρ_0 distribution while the bottom plot shows the f_0 and f_2 distributions. The error bars are the sum of the statistical and systematic errors*

- The track pseudorapidity boundary value was allowed to change from $|\eta| = 1.3$ to $|\eta| = 1.0$, the first being the minimal cut to get a reasonable signal and the latter giving the best possible geometric acceptance.
- The assumed f_0 width in the fit was varied in the accepted range of the PDG [16], from 40 MeV to 100 MeV.
- The photon virtuality, Q^2 , was varied between 2 GeV² and 4 GeV², the first being the Q^2 cut of the Monte Carlo and the latter being a known cut value between DIS and photoproduction at ZEUS.
- The reflection normalisation was varied between 0.05 and 0.15.

The normalisation of the reflections was found to have no effect on the cross section; the value stayed the same for a reasonable variation. It then has no contribution in the systematic errors. Other sources of systematic uncertainties could have been addressed here, such as variation of the MC generator, different production modes for the mesons, but they were not considered here since only one MC sample was used.

6.5 Discussion

The inclusive ρ^0 , f_0 and f_2 meson resonances production has been measured with the ZEUS detector. Within the range $Q^2 > 3 \text{ GeV}^2$, $|\eta| < 1.3$ and $p_T > 150 \text{ MeV}$, the total cross sections were calculated and the results are presented in equation 6.15. The differential p_T and η cross sections were measured and are presented in tables 6.4 and 6.3. The total cross section for each signal, in particular for the f_2 meson with $\sigma > 0.3 \text{ nb}$, is a clear indication that the particle was observed [18].

The shape of the differential cross sections is in agreement with those measured by H1 in photoproduction [17] (see figure 6.10). The total cross sections for each meson were not measured by H1 so we cannot compare. The differential η cross section is flat within errors, showing that there is no spatial dependence nor rapidity gap for the production of these neutral meson resonances in deep inelastic scattering. Also, the differential p_T cross section is decreasing as expected.

The cross sections could not be compared to a theoretical model since the Monte Carlo did not describe the f_0 and f_2 mesons. In order to compute detector corrections, the acceptance of pion pairs in the selected mass region was used. A more reliable measurement of the f resonances would need the simulation to include them. It is reasonable to say that the acceptances would then be lower than those measured with the pion pairs method. Hence the cross sections measured in this analysis are giving a clearer indication for the production of these resonances since the real values are probably even higher.

H1 prelim.

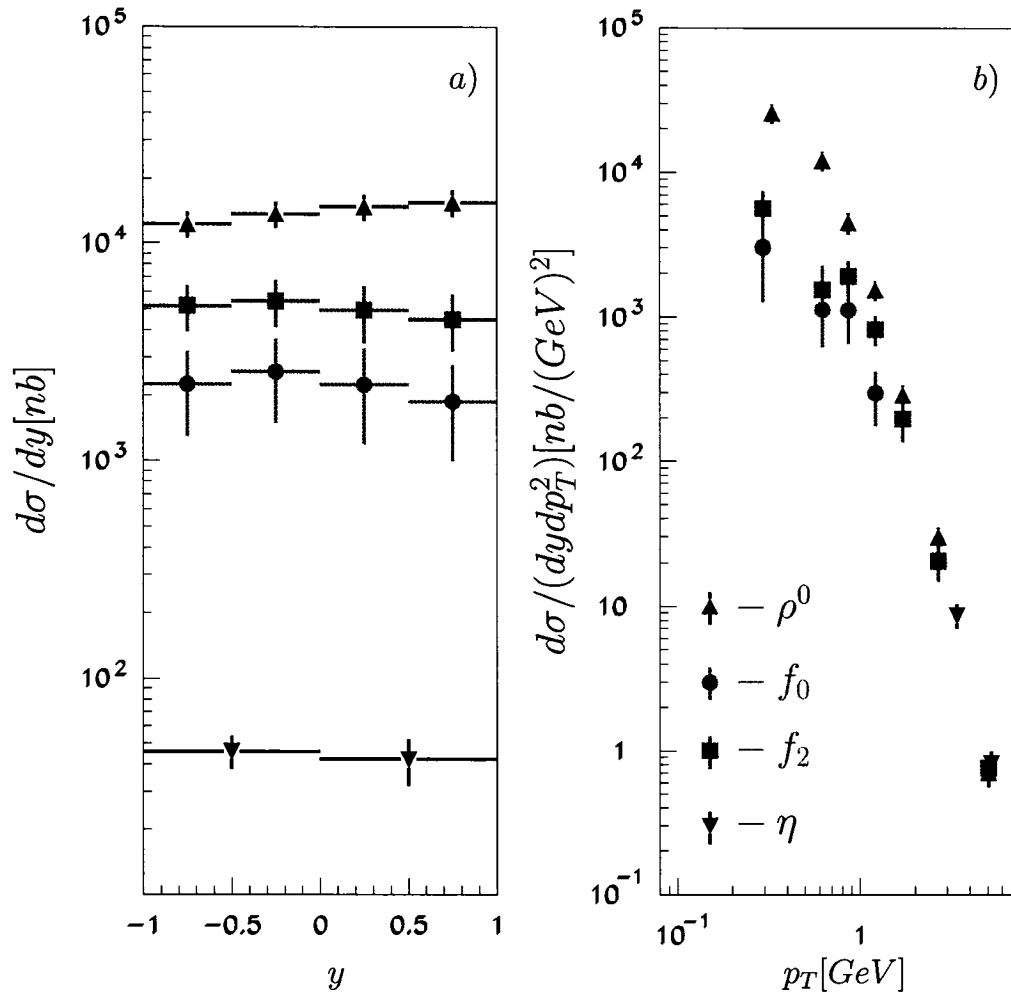


Figure 6.10: Differential cross sections measured by the H1 collaboration for η , ρ^0 , f_0 and f_2 mesons. [17]

7 Conclusion and Outlook

The measurement of the inclusive cross sections of the three neutral resonances ρ^0 , f_0 and f_2 was performed with the ZEUS detector for the running period 1998-2000, which corresponds to an integrated luminosity of 82.5 nb^{-1} . The differential cross sections were measured as functions of p_T and η . The values for the total cross sections show clearly the existence of these three particles, especially for the f resonances. In order to give an indication as to how the f_2 meson is produced, a total cross section of at least 0.3 nb had to be measured according to [18]. This was achieved in this analysis.

The differential cross sections as a function of the meson transverse momentum and pseudorapidity were measured. The $d\sigma/d\eta$ measurement reveals no dependence in pseudorapidity while the $d\sigma/dp_T$ measurement shows a decreasing cross section with increasing transverse momentum, as expected.

In order to have a better measurement of these cross sections, for study of resonance production mechanism, a simulation of the f resonances would be necessary. The detector corrections for these two resonances could then be extracted with accuracy and it is a reasonable assumption to say that they would be smaller than 100 %, hence increasing the measured values for the total cross sections. Also, better statistics could obviously reduce the statistical errors, hence giving more precise results. Finally, the method could be improved by doing a global fit that would include the background, the signals and the reflections all at once. This would reduce the sources of systematic errors by reducing it to the errors on the fit parameters and keep the correlations.

The similarities in behaviour between long-lived and short-lived hadrons, or resonances, could have been also studied with the present data if the double differential cross section in pseudorapidity and transverse momentum would have been calculated. It would be interesting to compare with the H1 results on that subject. A better understanding of the measured cross sections would require further studies on the ρ^0 meson shifted mass peak value. The hypoth-

esis that it is caused by the Bose-Einstein Correlations is not the only possible option, as was proposed by the experiments on the LEP collider [48]. If these resonances are also seen at heavy ion collision experiments, they can be also explained by the formation of a quark-gluon plasma.

Glossary

ADAMO	Aleph DATA MOdel: Entity relationship language used to store data
ARIADNE	Parton Shower program for Monte Carlo simulations
BAC	Backing Calorimeter
BCAL	Barrel Calorimeter
BFKL	Balitsky-Fadin-Kuraev-Lipatov: evolution scheme equations
C5	Radiation counter on the beamline in the electron direction
CAL	Calorimeter
CC	Charged Current
CTD	Central Tracking Detector
CTEQ5L	Parton Distribution Function set developed by the Coordinated Theoretical-Experiment project on QCD group
DESY	Deutsches Elektronen SYNchrotron
DGLAP	Dokshitzer-Gribov-Lipatov-Altarelli-Parisi: evolution scheme equations
DIS	Deep Inelastic Scattering
DJANGO	Monte Carlo generator for deep inelastic scattering events
DST	Data Summary Tape
DU	Depleted Uranium
EFO	Energy Flow Object
EMC	Electromagnetic calorimeter cells
EVB	Event Builder
FADC	Flash Analog to Digital Converters
FC	Fast Clear
FCAL	Forward Calorimeter
FDET	Forward Detector
FLT	First Level Trigger
FTD	Forward Tracking Device

GEANT	CERN routine that simulates volumes and passage of particles through matter
GFLT	Global First Level Trigger
GSLT	Global Second Level Trigger
HAC	Hadronic calorimeter cells
HERA	Hadron Elektron Ring Anlage
HERACLES	Monte Carlo generator for DIS events
HERWIG	Hadron Emission Reactions With Interfering Gluons, a Monte Carlo generator
IP	Interaction Point
IR	Infrared Divergencies
ISR	Initial State Radiation
LEPTO	Fragmentation program for Monte Carlo simulations
LLA	Leading Logarithm Approximation
LO	Leading Order
LUMI	Luminosity Monitor
MC	Monte Carlo simulations
MOZART	MONte Carlo for Zeus Analysis, Reconstruction and Trigger
MVD	Micro Vertex Detector
NC	Neutral Current
NLLA	Next-to-Leading Logarithm Approximation
NLO	Next-to-Leading Order
PDF	Parton Distribution Function
PIA	Positron Intensity Accumulator
PMT	Photomultiplier tube
pQCD	Perturbative Quantum Chromodynamics
QCD	Quantum Chromodynamics
QED	Quantum Electrodynamics
QFT	Quantum Field Theory
QPM	Quark Parton Model
RCAL	Rear Calorimeter
RTD	Rear Tracking Device
SCSN-38	Polystyrene material used for scintillator plates

SINISTRA	Neural network based electron finder
SL	Superlayer in the CTD
SLT	Second Level Trigger
SRTD	Small Rear angle Tracking Detector
TLT	Third Level Trigger
TRD	Transition Radiation Detector
VXD	Vertex Detector
ZEPHYR	ZEus PHYSics Reconstruction
ZGANA	Zeus GEANT ANALysis: the Zeus Trigger Simulation

References

- [1] D. J. Gross and Frank Wilczek. Ultraviolet Behavior of Non-Abelian Gauge Theories. *Phys. Rev. Lett.*, 30:1343–1346, 1973.
H. David Politzer. Reliable Perturbative Results for Strong Interactions. *Phys. Rev. Lett.*, 30:1346–1349, 1973.
- [2] J.B. Birks, editor. *Rutherford at Manchester*. Heywood and Co, 1962.
- [3] M. Gell-Mann and Y. Ne'eman. *The Eightfold Way*. W. A. Benjamin, 1964.
- [4] J. D. Bjorken and Emmanuel A. Paschos. Inelastic electron proton and gamma proton scattering, and the structure of the nucleon. *Phys. Rev.*, 185:1975–1982, 1969.
- [5] E. D. Bloom et al. Recent Results in Inelastic Electron Scattering. SLAC-PUB-796, 1970.
- [6] Curtis G. Callan and David J. Gross. High-energy electroproduction and the constitution of the electric current. *Phys. Rev. Lett.*, 22:156–159, 1969.
- [7] Günther Dissertori et al. *Quantum Chromodynamics: High Energy Experiments and Theory*. Oxford Science Publications, 2003.
- [8] Stephan Narison. *QCD as a Theory of Hadrons*. Cambridge University Press, 2004.
- [9] O. W. Greenberg. Spin and Unitary Spin Independence in a Paraquark Model of Baryons and Mesons. *Phys. Rev. Lett.*, 13:598–602, 1964.
- [10] Günter Wolf. HERA Physics. DESY 94-022, 1994.
- [11] R. P. Feynman. Space-time approach to quantum electrodynamics. *Phys. Rev.*, 76:769–789, 1949.
- [12] Guido Altarelli and G. Parisi. Asymptotic freedom in parton language. *Nucl. Phys.*, B126:298, 1977.

- Yuri L. Dokshitzer. Calculation of the structure functions for deep inelastic scattering and $e^+ e^-$ annihilation by perturbation theory in quantum chromodynamics. (in russian). *Sov. Phys. JETP*, 46:641–653, 1977.
- L. N. Lipatov. The parton model and perturbation theory. *Sov. J. Nucl. Phys.*, 20:94–102, 1975.
- V. N. Gribov and L. N. Lipatov. Deep inelastic $e p$ scattering in perturbation theory. *Sov. J. Nucl. Phys.*, 15:438–450, 1972.
- [13] E. A. Kuraev, L. N. Lipatov, and Victor S. Fadin. The pomeron singularity in nonabelian gauge theories. *Sov. Phys. JETP*, 45:199–204, 1977.
- I. I. Balitsky and L. N. Lipatov. The pomeron singularity in quantum chromodynamics. *Sov. J. Nucl. Phys.*, 28:822–829, 1978.
- [14] Sabine Lammers. *A Study of Parton Dynamics at Low x with ZEUS at HERA*. PhD thesis, University of Wisconsin-Madison, 2004.
- [15] I. P. Ivanov. The hard scale in the exclusive rho meson production in diffractive dis. *Phys. Rev.*, D68:032001, 2003.
- [16] Particle Data Group. Particle physics booklet, 2004. Reprinted from Physics Letters B592.
- [17] H1 collaboration. Measurements of the Inclusive Photoproduction of η , ρ^0 , $f_0(980)$ and $f_2(1270)$ Mesons at HERA. H1prelim-03-037, 2003.
- [18] E. R. Berger, A. Donnachie, H. G. Dosch, and O. Nachtmann. Observing the odderon: Tensor meson photoproduction. *Eur. Phys. J.*, C14:673–682, 2000.
- [19] ZEUS Collaboration. The Zeus Detector: Status Report 1993. Technical report, DESY, 1993.
- [20] HERA. A Proposal for a large Electron-Proton Colliding Beam Facility at DESY. Technical report, DESY, 1981. DESY-HERA 81-10.
- [21] K. Sasahara et al. Positron production from a tungsten single crystal at the KEK 8-GeV electron linac. Prepared for 21st ICFA Beam Dynamics

- Workshop on Laser Beam Interactions, Stony Brook, New York, 11-15 Jun 2001.
- [22] B. Foster et al. The Design and Construction of the ZEUS Central Tracking Detector. *Nucl. Instrum. Meth.*, A338:254–283, 1994.
- B. Foster et al. The performance of the ZEUS central tracking detector z-by-timing electronics in a transputer based data acquisition system. *Nucl. Phys. B Proc. Suppl.*, 32:181–188, 1993.
- [23] D. S. Bailey et al. The design and performance of the ZEUS central tracking detector z-by-timing system. *Nucl. Instrum. Meth.*, A396:320–349, 1997.
- [24] G.F. Hartner, Y. Iga, J.B. Lane, N.A. McCubbin, M. Wing. VCTRACK Offline Output Information. ZEUS-NOTE-97-064, 1997.
- [25] CERN Programming Techniques Group, ECP Division. *ADAMO: Entity-Relationship Programming System, Version 3.3*, 1993.
- [26] P. Billoir and S. Qian. Fast vertex fitting with a local parametrization of tracks. *Nucl. Instrum. Meth.*, A311:139–150, 1992.
- [27] A. Andresen et al. Construction and beam test of the ZEUS forward and rear calorimeter. *Nucl. Instrum. Meth.*, A309:101–142, 1991.
- A. Bernstein et al. Beam tests of the ZEUS barrel calorimeter. *Nucl. Instrum. Meth.*, A336:23–52, 1993.
- M. Derrick et al. Design and construction of the ZEUS barrel calorimeter. *Nucl. Instrum. Meth.*, A309:77–100, 1991.
- [28] J. Andruszkow et al. First Measurements of HERA Luminosity by ZEUS Lumi Monitor. DESY 92-066, May 1992.
- [29] H. Bethe and W. Heitler. On the Stopping of Fast Particles and Creation of Electron Pairs. *Proc. Roy. Soc.*, A146:83–112, 1934.
- [30] C. Youngman. The ZEUS data acquisition system. In *International Conference on Computing in High-Energy Physics, 10th, CHEP 92. Pro-*

- ceedings, Annecy, France, September 21-25, 1992*, pages 145–150, 1992. CERN 92-07.
- W. H. Smith, K. Tokushuku, and L. W. Wiggers. The ZEUS trigger system. In *International Conference on Computing in High-Energy Physics, 10th, CHEP 92. Proceedings, Annecy, France, September 21-25, 1992*, pages 222–225, 1992. CERN 92-07.
- [31] H. Boterenbrood et al. A Two transputer VME module for data acquisition and online event selection in ZEUS. *Nucl. Instrum. Meth.*, A332:263–268, 1993.
- [32] Liang Li. *Three jet production in neutral current deep inelastic scattering with ZEUS at HERA*. PhD thesis, University of Wisconsin, 2005.
- [33] Amita Raval. Private communication.
- [34] Elisabetta Gallo. The TLT and DST filters for the DIS group in 1995. ZEUS 96-001, 1996.
- Steve James Henry Hanlon. *Measurement of Event Shapes in Deep Inelastic Scattering at HERA*. PhD thesis, University of Glasgow, 2004.
- [35] Niels Tuning. *Proton Structure Function at HERA*. PhD thesis, University of Amsterdam/NIKHEF, 2001.
- [36] Halina Abramowicz, Allen Caldwell, and Ralph Sinkus. Neural network based electron identification in the ZEUS calorimeter. *Nucl. Instrum. Meth.*, A365:508–517, 1995.
- [37] F. Jacquet and A. Blondel. Detection and study of the charged current event. In U. Amaldi, editor, *Proceedings of the Study of an ep facility for Europe: DESY Hamburg, April 2-3, 1979*, pages 391–396, 1979. DESY-79-48.
- [38] Sanjay Padhi. *Charm Jets in Photoproduction*. PhD thesis, McGill University, 2004.
- [39] G. A. Schuler and H. Spiesberger. DJANGO: the interface for the event generators HERACLES and LEPTO. In *Physics at HERA: volume 3*,

- pages 1419–1432, 1992. Proceedings of the Workshop, Hamburg, Oct. 29-30, 1991.
- [40] A. Kwiatkowski, H. Spiesberger and H.-J. Möhring. HERACLES. An Event Generator for ep Interactions at HERA Including Radiative Processes. In *Physics at HERA: volume 3*, pages 1294–1310, 1992. Proceedings of the Workshop, Hamburg, Oct. 29-30, 1991.
- [41] G. Ingelman. LEPTO version 6.1 - The Lund Monte Carlo for Deep Inelastic Lepton-Nucleon Scattering . In *Physics at HERA: volume 3*, pages 1366–1394, 1992. Proceedings of the Workshop, Hamburg, Oct. 29-30, 1991.
- [42] H. L. Lai et al. Global QCD analysis of parton structure of the nucleon: CTEQ5 parton distributions. *Eur. Phys. J.*, C12:375–392, 2000.
- [43] L. Lönnblad. Ariadne version 4. In *Physics at HERA: volume 3*, pages 1440–1445, 1992. Proceedings of the Workshop, Hamburg, Oct. 29-30, 1991.
- [44] Gosta Gustafson and Ulf Pettersson. Dipole formulation of QCD cascades. *Nucl. Phys.*, B306:746, 1988.
- [45] Bo Andersson, G. Gustafson, G. Ingelman, and T. Sjostrand. Parton fragmentation and string dynamics. *Phys. Rept.*, 97:31, 1983.
- [46] R. Brun et al. Geant 3.13, 1987. CERN DD/EE/84-1.
- [47] J. D. Jackson. Remarks on the phenomenological analysis of resonances. *Nuovo Cim.*, 34:1644–1666, 1964.
- [48] G. D. Lafferty. Residual Bose-Einstein correlations in inclusive $\pi^+\pi^-$ systems and the $\rho^0(770)$ line shape in multi-hadronic Z^0 decay. *Z. Phys.*, C60:659–666, 1993.
- P. Abreu et al. Production characteristics of K^0 and light meson resonances in hadronic decays of the Z^0 . *Z. Phys.*, C65:587–602, 1995.